AGU PUBLICATIONS

JGR

Journal of Geophysical Research: Earth Surface

RESEARCH ARTICLE
10.1002/2015JF003708

Key Points:
- Variability in glacier dynamics of the Canadian Arctic
- Variability in dynamic discharge from the Canadian Arctic
- Distinction between mechanisms controlling glacier dynamics within the Canadian Arctic

Correspondence to:
W. Van Wychen,
wvanw046@uottawa.ca

Citation:
Van Wychen, W., J. Davis, D. O. Burgess, L. Copland, L. Gray, M. Sharp, and C. Mortimer (2016), Characterizing interannual variability of glacier dynamics and dynamic discharge (1999–2015) for the ice masses of Ellesmere and Axel Heiberg Islands, Nunavut, Canada, *J. Geophys. Res. Earth Surf.*, *121*, 39–63, doi:10.1002/2015JF003708.

Received 26 AUG 2015
Accepted 26 NOV 2015
Accepted article online 7 DEC 2015
Published online 14 JAN 2016

Characterizing interannual variability of glacier dynamics and dynamic discharge (1999–2015) for the ice masses of Ellesmere and Axel Heiberg Islands, Nunavut, Canada

Wesley Van Wychen[1,2], Jamie Davis[3], David O. Burgess[2], Luke Copland[1], Laurence Gray[1], Martin Sharp[3], and Colleen Mortimer[3]

[1]Department of Geography, Environment and Geomatics, University of Ottawa, Ottawa, Ontario, Canada, [2]Natural Resources Canada, Ottawa, Ontario, Canada, [3]Department of Earth and Atmospheric Sciences, University of Alberta, Edmonton, Alberta, Canada

Abstract Landsat 7 and RADARSAT-1/RADARSAT-2 satellite images are used to produce the most comprehensive record of glacier motion in the Canadian High Arctic to date and to characterize spatial and temporal variability in ice flow over the past ~15 years. This allows us to assess whether dynamically driven glacier change can be attributed to "surging" or "pulsing," or whether other mechanisms are involved. RADAR velocity mapping allows annual regional dynamic discharge (iceberg calving) to be calculated for 2000 and the period 2011–2015 (yielding a mean regional discharge of $2.21 \pm 0.68\,\mathrm{Gt\,a^{-1}}$), and velocities derived from feature tracking of optical imagery allow for annual dynamic discharge to be calculated for select glaciers from 1999 to 2010. Since ~2011, several of the major tidewater-terminating glaciers within the region have decelerated and their dynamic discharge has decreased. Trinity and Wykeham Glaciers (Prince of Wales Icefield) represent a notable departure from this pattern as they have generally accelerated over the study period. The resulting increase in dynamic discharge from these glaciers entirely compensates (within error limits) for the decrease in discharge from the other tidewater glaciers across the study region. These two glaciers accounted for ~62% of total regional dynamic discharge in winter 2015 (compared to ~22% in 2000), demonstrating that total ice discharge from the Canadian High Arctic can be sensitive to variations in flow of just a few tidewater glaciers.

1. Background and Study Site

The area of the ice masses of Axel Heiberg and Ellesmere Islands (Figure 1, inset) was ~89,000 $\mathrm{km^2}$ in ~2000, which is ~85% of the glacier area in the northern Canadian Arctic Archipelago [*Sharp et al.*, 2014; *Thomson et al.*, 2011]. *Van Wychen et al.* [2014] used winter 2012 RADARSAT-2 imagery to produce the first complete velocity maps and estimates of dynamic discharge from these ice masses (building on earlier regional measurements by *Short and Gray* [2005] and *Williamson et al.* [2008]). *Hattersley-Smith* [1969] and *Müller* [1969] described dynamic variability (attributed to surging) within the region as early as the 1960s. *Copland et al.* [2003a] identified at least 51 surge-type glaciers on Devon, Axel Heiberg, and Ellesmere Islands and provided the first comprehensive catalogue of the region's surge-type glaciers based on analysis of aerial photography (1959/1960) and Landsat 7 imagery (1999/2000). Together, these studies indicate that both glacier dynamics and iceberg discharge from the ice masses of Axel Heiberg and Ellesmere Islands vary both spatially and temporally.

There are several known mechanisms whereby glaciers in the Canadian Arctic can undergo dynamic changes on a seasonal basis. These include supraglacial hydrological forcing, whereby surface melt is transmitted to the bed, leading to enhanced glacier flow [e.g., *Bingham et al.*, 2003; *Boon and Sharp*, 2003; *Copland et al.*, 2003b] and, for tidewater-terminating glaciers, sea ice/mélange forcing, where reductions in sea ice/mélange strength reduce their buttressing effect on the glacier front, resulting in increased glacier velocities [e.g., *Williamson et al.*, 2008]. Oceanic forcing, where increases in ocean temperature drive increased melt rates at glacier termini leading to thinning and acceleration, has been identified in nearby Greenland [e.g., *Holland et al.*, 2008; *Murray et al.*, 2010; *Christoffersen et al.*, 2011] and may also influence glacier dynamics within the Canadian Arctic. However, the nature and causes of tidewater glacier velocity variability have not been well investigated in the Canadian Arctic, and most previously observed variations in the motion of tidewater glaciers

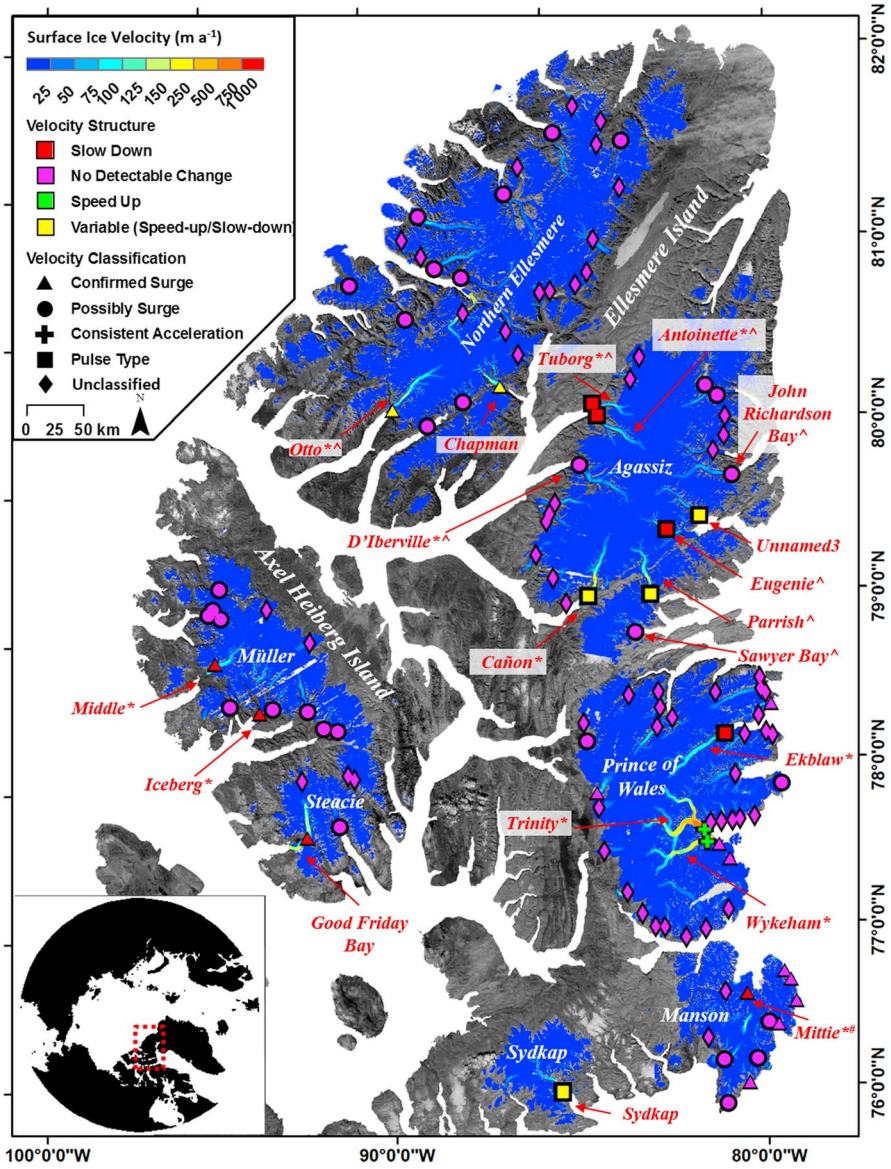

Figure 1. Distribution of dynamic changes and velocity classification for major glaciers included in this study. Asterisk indicates glaciers with previous velocity maps derived by *Short and Gray* [2005], circumflex accent derived by *Williamson et al.* [2008], and number sign derived by *Copland et al.* [2003a]. Background glacier velocities derived by speckle tracking of RADARSAT-2 imagery acquired in winter 2015 (exact imaging dates are provided in Table 1).

have either been attributed to surging [e.g., *Van Wychen et al.*, 2012; *Copland et al.*, 2003a] or remain unexplained due to a lack of multiyear observations.

Surge-type glaciers undergo a cyclic behavior, with periods of rapid acceleration and advance (active phase) followed by periods of slow flow where ice fluxes are less than balance fluxes (quiescent phase) [*Clarke*, 1987; *Benn and Evans*, 2010]. Differences in the duration of the active and quiescent phases observed on surge-type glaciers in Alaska and Svalbard have led to the classification of surge-type glaciers as either "Alaskan type" or "Svalbard type" [*Benn and Evans*, 2010] and to speculation that there may be different mechanisms of surge initiation for the two types. The relatively short active (~1–4 years) and quiescent (~35–40 years) phases of Alaskan-type surge-type glaciers, combined with surge termination that is coincident with large outburst floods, suggest that buildup of water pressure in a linked-cavity subglacial drainage system plays an important role in the initiation of surges of these glaciers [*Kamb*, 1987; *Murray et al.*, 2003]. The longer active (~7–15 years) and quiescent (~50–100 years) phases of Svalbard-type surge-type glaciers, combined with surge termination that

occurs over a multiyear period [*Dowdeswell et al.*, 1991; *Murray et al.*, 1998], suggest that these surges are linked to changes in basal thermal conditions rather than subglacial water pressure [*Murray et al.*, 2003]. The longer active phases reported on land-terminating glaciers in the Canadian Arctic (e.g., at least 10 years for Good Friday Bay Glacier) led *Copland et al.* [2003a] to surmise that surge-type behavior within the Canadian Arctic was likely similar to Svalbard-type surge-type glaciers.

A major limitation of earlier studies of variability in glacier motion within the Canadian Arctic is that dynamic change has largely been inferred rather than measured. In those cases where glacier velocities have been measured, measurements have been limited to short time periods (e.g., glacier velocities were only measured over 1–3 years). As a result, the spatial and temporal scales of variability in glacier dynamics have not been well constrained. This hinders identification of the mechanisms responsible for variability in ice flow within the region. Understanding the processes that are responsible for regulating ice flow is of paramount importance for explaining how and why mass loss via dynamic discharge varies over time, and for accurately projecting future contributions to sea level rise from the Canadian Arctic.

We produced surface velocity maps for all ice-covered terrain on Axel Heiberg and Ellesmere Islands from RADARSAT-1 fine beam data (8 m resolution; 2000 and 2006–2007) and RADARSAT-2 fine and ultrafine beam data (8 m and 3 m resolution; 2009–2014) (Table 1). Feature tracking of Landsat 7 Enhanced Thematic Mapper Plus (ETM+; 15 m resolution) imagery from 1999 to 2010 was also used to determine the motion of ~14–16 glaciers to extend the spatial and temporal record of ice motion (Table 1). We use this ~15 year record of ice motion to quantify the timescale and magnitude of glacier dynamic fluctuations across the Canadian Arctic for the first time. This record is augmented with a record of glacier terminus positions (derived from manual inspection of optical imagery) to provide insight into the mechanisms that are driving the dynamic changes. Where available, we compare glacier bed, ice thickness, and surface elevation profiles to understand topographic conditions in regions where velocity variability occurs and identify features (e.g., basal topographic features) that may be regulating ice motion. Additionally, the derived velocities are combined with measurements of the ice thickness of major outlet glaciers to estimate the regional dynamic discharge in 2000 and from 2011 to 2015 and for select glaciers with available velocity data from 1999 to 2010. Here we define dynamic discharge (sometimes termed iceberg calving or frontal ablation in other studies) as the mass of ice passing through a fixed terminus flux gate, which does not account for the effect on ice flux from terminus advance or retreat.

2. Methods and Data

2.1. Satellite Imagery

RADARSAT-1 imagery for the year 2000 was obtained from Alaska Satellite Facility's Vertex Data Portal (https://vertex.daac.asf.alaska.edu/) and for 2006 to 2008 from archives held by the Geological Survey of Canada. All RADARSAT-1 imagery was obtained in level 0 CEOS format and processed to single look complex images with GAMMA Modular SAR Processor software. RADARSAT-2 data were obtained through Natural Resources Canada's RADARSAT-2 Government Data Allocation administered by the Canadian Space Agency. Nearly all RADARSAT-1 and RADARSAT-2 scenes were acquired from middle fall to early spring (November–April), when the glacier surface remains relatively undisturbed between image acquisitions (e.g., snowfall is minimal, and melting is rare). This increases the likelihood that the selected images will produce reliable velocity measurements.

Cloud-free and snow-free panchromatic (band 8) Landsat 7 Enhanced Thematic Mapper Plus (ETM+) images from 1999 to 2010 (used for feature tracking) and multispectral Landsat 8 Operational Land Imager (OLI) (used to derive terminus positions in 2013–2014) were obtained from the United States Geological Survey (USGS) data portal (http://earthexplorer.usgs.gov/). Cloud-free and minimal snow cover ASTER (Advanced Spaceborne Thermal Emission and Reflection Radiometer) L1B data (used to derive terminus positions and identify surface features indicative of surging from 2000 to 2012) were obtained from NASA's online data portal (http://reverb.echo.nasa.gov/). All Landsat 7/Landsat 8 imagery was preprocessed with the USGS Level 1 product generation system that includes radiometric and geometric correction and transformation to the Universal Transverse Mercator projection. Due to the scan line corrector failure of Landsat 7, stripes occur across the noncentral parts of imagery after 31 May 2003. Although estimates of surface velocities derived in the study are not affected by the data gaps [*Haug et al.*, 2010], images that minimize data gaps were

Journal of Geophysical Research: Earth Surface

10.1002/2015JF003708

Table 1. Summary of Remote Sensing Imagery Used in This Study[a]

	Image 1	Image 2		Image 1	Image 2		Image 1	Image 2		Image 1	Image 2		Image 1	Image 2	
SAR Imagery (Speckle Tracking: DD/MM/YY Image Segments)															
Northern Ellesmere	20/10/00	13/11/00	1	16/12/00	09/01/01	4	25/02/07	21/03/07	1	13/01/11	06/02/11	4	16/01/14	09/02/14	2
	30/10/00	23/11/00	3	19/12/00	12/01/01	1	18/03/08	11/04/08	1	26/01/11	19/02/11	5	17/01/14	10/02/14	3
	03/11/00	21/12/00	1	19/12/00	12/01/01	1	13/04/09	07/05/09	1	27/01/11	20/02/11	4	11/01/15	04/02/15	3
	12/11/00	30/12/00	3	21/12/00	14/01/01	1	20/02/10	16/03/10	1	30/01/11	23/02/11	5	01/03/15	25/03/15	3
	21/11/00	15/12/00	2	23/12/00	16/01/01	1	07/01/11	31/01/11	2	01/02/11	25/02/11	4			
	12/12/00	05/01/01	2	02/03/06	26/03/06	1	10/01/11	03/02/11	4	27/01/12	20/02/12	2			
	13/12/00	06/01/01	2	09/03/06	02/04/06	1	11/01/11	04/02/11	5	28/01/12	21/02/12	3			
Prince of Wales	14/10/00	07/11/00	1	18/12/00	11/01/01	2	28/02/07	24/03/07	1	26/01/11	19/02/11	3	07/12/13	31/12/13	2
	17/10/00	10/11/00	4	28/12/00	21/01/01	1	18/03/08	11/04/08	1	22/02/11	18/03/11	5	08/12/13	01/01/14	2
	21/11/00	08/01/01	1	29/12/00	22/01/01	2	01/04/08	25/04/08	1	25/02/11	21/03/11	5	03/12/14	27/12/14	2
	28/11/00	15/01/01	1	23/02/06	19/03/06	1	19/02/09	15/03/09	1	09/04/12	03/05/12	2	26/12/14	19/01/15	2
	01/12/00	25/12/00	2	05/03/06	22/04/06	1	01/03/09	25/03/09	1	05/01/13	29/01/13	2			
	08/12/00	01/01/01	1	18/02/07	14/03/07	1	25/02/10	21/03/10	2	06/01/13	30/01/13	1			
Agassiz	04/12/00	28/12/00	1	09/12/00	02/01/01	1	03/03/07	27/03/07	1	11/03/10	04/04/10	1	06/01/13	30/01/13	2
	08/11/00	02/12/00	1	16/12/00	09/01/01	3	06/03/07	30/03/07	1	01/01/11	25/01/11	3	24/01/14	17/02/14	2
	09/11/00	03/12/00	1	29/12/00	22/01/01	2	28/04/08	22/05/08	1	05/01/11	29/01/11	3	25/01/14	18/02/14	1
	27/12/00	20/01/01	1	23/12/00	16/01/01	1	05/03/09	29/03/09	1	08/01/11	01/02/11	5	03/12/14	27/12/14	2
	30/12/00	23/01/01	3	23/02/06	19/03/06	1	31/03/09	24/04/09	2	12/01/12	05/02/12	1			
	28/12/00	21/01/01	3	11/03/06	04/04/06	1	23/02/10	18/03/10	1	09/04/12	03/05/12	2			
Müller and Steacie	17/12/00	10/01/01	5	01/03/07	25/03/07	1	29/04/08	23/05/08	1	01/02/11	25/02/11	3	04/01/13	28/01/13	2
	20/12/00	13/01/01	1	02/03/07	26/03/07	1	17/02/09	13/03/09	1	18/02/11	14/03/11	3	23/01/14	18/02/14	2
	06/03/06	30/03/06	5	05/03/07	29/03/07	1	05/03/09	29/03/09	1	27/02/12	22/03/12	3	18/01/15	11/02/15	2
Manson	14/10/00	07/11/00	1	04/03/07	28/03/07	1	09/04/12	03/05/12	1	07/12/14	31/12/14	1	12/02/15	08/03/15	1
	18/12/00	11/01/01	1	15/03/08	08/04/08	1	05/01/13	29/01/13	1						
Sydkap	27/2/12	22/03/12	1	30/01/13	23/02/13	1	08/12/13	01/01/14	1	03/12/14	27/12/14	1			
Landsat 7 Imagery (Feature Tracking: DD/MM/YY Path-Row)															
Northern Ellesmere	02/07/99 57-1	18/06/00 57-1		14/06/01 56-1	17/06/02 56-1		25/07/05 58-1	05/07/06 57-1		22/07/07 59-1	10/07/08 58-1		25/06/09 59-1	28/06/10 59-1	
	08/06/00 57-1	14/06/01 56-1		13/06/04 57-1	25/07/05 58-1		05/07/06 57-1	22/07/07 59-1		10/07/08 58-1	25/06/09 59-1				
Prince of Wales	09/07/99 42-4	27/06/00 40-4		22/07/03 42-4	17/07/04 39-4		07/06/05 42-4	10/06/06 42-4		24/07/07 41-4	01/07/08 42-4		17/06/08 40-4	11/06/09 41-4	
	27/06/00 40-4	12/06/01 42-4		04/06/04 40-4	23/06/05 42-4		09/07/05 42-4	28/07/06 42-4		24/07/07 41-4	10/07/08 41-4		11/06/09 41-4	30/06/10 41-4	
	12/06/01 42-4	15/06/02 42-4		04/06/04 40-4	09/06/05 42-4		28/07/06 42-4	27/07/07 42-4		01/07/08 41-4	13/07/09 41-4		13/07/09 41-4	06/06/10 41-4	
	15/06/02 42-4	22/07/03 40-4													
Agassiz	03/07/99 48-2	28/06/00 47-2		17/06/01 45-3	02/07/02 49-2		16/07/03 46-2	11/07/04 45-3		02/07/06 48-2	12/07/07 48-2		27/06/08 46-2	16/07/09 46-2	
	08/07/99 51-1	24/06/00 51-1		11/06/01 51-1	19/06/02 54-1		21/06/04 49-2	28/07/05 47-2		08/07/06 46-3	27/07/07 46-2		16/07/09 46-2	03/07/10 46-2	
	10/07/99 49-2	28/06/00 47-2		15/06/01 47-2	11/06/02 46-2		19/07/04 53-1	15/07/05 52-1		25/07/07 48-2	04/07/08 47-5		16/07/09 46-2	26/07/10 47-2	
	03/07/99 48-2	28/06/00 47-2		02/07/02 49-2	18/07/03 44-3		11/07/04 45-3	05/07/05 46-2		12/07/07 53-1	28/06/08 53-1		14/07/09 48-2	01/07/10 48-2	
	05/07/99 46-2	28/06/00 47-2		01/08/02 51-1	26/07/03 52-1		28/07/05 47-2	06/07/06 48-2		11/07/07 46-2	27/06/08 46-2		10/07/09 52-1	14/08/10 52-1	
	28/06/00 47-2	15/06/01 47-2		02/07/02 49-2	16/07/03 46-2		20/06/05 53-1	02/07/06 52-1		04/07/08 47-2	14/07/09 48-2				
	24/06/00 51-1	11/06/01 51-1		18/07/03 44-3	21/06/04 49-2		05/07/05 46-2	08/07/06 46-2		28/06/08 53-1	10/07/09 52-1				
	28/06/00 48-2	15/06/01 47-2		26/07/03 52-1	19/07/04 53-1		06/07/06 48-2	25/07/07 48-2		27/06/08 46-2	14/06/09 46-2				
Müller and Steacie	23/07/99 60-2	18/06/00 57-2		26/06/01 60-2	06/06/02 59-2		02/06/05 55-3	07/07/06 55-3		10/07/07 55-3	12/07/08 55-3		13/07/09 57-2	30/06/10 57-2	
	18/06/00 57-2	26/06/01 60-2		15/06/04 55-3	02/06/05 55-3		07/07/06 55-3	10/07/07 55-3		12/07/08 55-3	15/07/09 55-3				
Sydkap	02/07/99 41-5	18/06/00 41-5		23/05/02 41-6	26/05/03 41-6		04/06/04 42-5	07/06/05 42-5		10/06/06 42-5	29/06/07 42-5		01/07/08 42-5	18/06/09 42-5	
	09/06/00 42-5	12/06/01 42-5		26/05/03 41-6	04/06/04 42-5		07/06/05 42-5	10/06/06 42-5		29/06/07 42-5	01/07/08 42-5		18/06/09 42-5	07/07/10 42-5	
	12/06/01 42-5	13/06/02 44-5													
Manson	13/07/99 38-5	29/06/00 38-5		19/07/02 40-5	11/08/03 36-6		10/07/04 39-5	04/07/05 38-5		30/06/06 38-5	03/07/07 38-5		21/07/08 38-5	22/07/09 40-5	
	11/06/00 40-5	14/06/01 40-5		11/08/03 36-6	17/07/04 39-5		04/07/05 39-5	30/06/06 38-5		03/07/07 38-5	05/07/08 38-5		29/06/09 39-5	23/06/10 40-5	
	14/06/01 40-5	10/06/02 39-5													

Table 1. (continued)

	Image 1	Image 2	Image 1	Image 2	Image 1	Image 2	Image 1	Image 2	Image 1	Image 2
					ASTER/Landsat 8 (Terminus Position: DD/MM/YY) (Path, Row provided for Landsat Imagery)					
Northern Ellesmere	25/06/00	28/09/03	01/06/04	03/07/06	22/07/07	26/07/09	15/08/10	03/07/11	30/06/12	24/08/14 46-248
	15/06/02	01/06/04								
Prince of Wales	18/04/01	27/04/03	24/07/04	12/04/08	13/06/10	02/07/12	01/08/12	06/08/13	22/08/14	07/09/14 39-4
	02/07/02	03/07/03	23/05/07	14/06/09						
Agassiz	29/07/00	03/07/02	19/07/04	20/06/05	11/07/07	26/06/09	27/07/10	09/06/11	06/08/12	13/06/13
	18/08/01	04/08/03	20/06/05	30/06/06	07/08/07	25/07/09	21/06/10	01/07/11	31/07/13	25/08/14 45-3
	19/07/01	27/06/04	14/08/05	09/07/06	13/05/08	24/07/10				
Müller and Steacie	22/07/00	19/08/01	01/07/02	24/07/04	12/08/05	23/04/07	13/08/10	23/09/11	20/09/12	18/08/14 88-242
	29/07/00	25/05/02	11/07/03	29/07/05	09/07/06	19/09/10	05/07/10	15/09/12	12/08/14 51-4	24/08/14 52-3
	20/07/01	16/07/02	27/06/03							
Manson	27/06/00	12/07/03	26/07/04	29/06/06	30/07/09	17/08/12	30/07/13	22/08/14 36-6		
Sydkap	18/04/01	10/05/02	17/08/06	17/08/07	16/08/14 40-6					

[a]SAR image pairs from 2000 to 2008 were RADARSAT-1 fine beam (9 m resolution); from 2009 to 2011 RADARSAT-2 fine beam (9 m resolution); from 2011 to 2014 RADARSAT-2 wide fine beam (9 m resolution).

preferentially selected. Imagery from the summer and early fall (approximately May to September) was selected to minimize snow cover. Temporal variability or shifts in the timing of peak melt could have impacted the ice surface velocities derived from Landsat 7 image pairs, either because the peak melt events in both of two successive summers occurred within the time window between image acquisitions or because neither summer peak melt event occurred within the time window between successive image acquisitions. However, due to the limited number of cloud-free scenes available for velocity determination and a paucity of in situ data from which to determine when peak melt occurred on each individual glacier in each year, Landsat 7 imagery separated by ~365 days was selected for the analysis in order to minimize the effect of seasonal velocity fluctuations on estimates of annual mean displacement. An inventory of imagery used in this study is provided in Table 1.

2.2. Determination of Ice Motion

We determine ice motion using speckle tracking for RADAR imagery acquired during a single winter season and feature tracking for Landsat summer imagery acquired at ~1 year intervals. As a consequence, we refer to velocities derived from RADAR imagery as "winter velocities" (although the results are extrapolated to annual values) and to those derived from Landsat imagery as "annual velocities" in order to distinguish between the two. We expect a discrepancy between the two data sets, as the annual velocities are likely to include spring/summer speedups that increase total annual motion relative to that which would be derived by extrapolation of winter velocities.

2.2.1. Speckle Tracking of RADARSAT Data

Surface ice motion was determined using custom speckle tracking code written in MATLAB™ for both RADARSAT-1 and RADARSAT-2 data sets [*Van Wychen et al.*, 2012, 2014; *Short and Gray*, 2005]. This code utilizes a cross-correlation algorithm on image chips from coregistered 24 day or 48 day image pairs to determine the relative displacement of features between scenes. Due to poorer orbital knowledge of RADARSAT-1 relative to RADARSAT-2, an additional manual coregistration of the RADARSAT-1 image pairs was required. This involved identification of features common to both the master and slave images to determine the offset between them. Overlapping image chips of ~450 m (101 pixels) in azimuth direction and ~850 m (101 pixels) in range were used to determine displacements. The 1:250,000 Canadian Digital Elevation data set, Level 1, was used to remove the range shift component which arises from the varying geometry across the swath. As the look angle varies, there is an additional displacement in slant range

that is proportional to the "perpendicular baseline" created by the two orbits [*Rosen et al*., 2000]. For example, with a RADARSAT fine mode pair and a relatively small perpendicular baseline of ~25 m, there is still a near-to-far cross-track displacement of ~ 1m. As varying topography also affects the look angle, the most convenient way to remove this unwanted component of range shift is to use a digital elevation model (DEM). Errors in the DEM have a small impact on the range shift correction and can normally be neglected. To remove systematic biases due to inaccuracies in satellite baseline estimates or squint effects between image acquisitions, displacements were calibrated using areas of zero motion (bedrock outcrops) to determine any systematic biases in the range or azimuth shifts, which were then removed from the rest of the data set.

Final displacements were standardized to annual values and imported into ArcGIS^{TM} 10.1 as vector data for verification. To identify and filter mismatches, manual checking of the data set was undertaken using the following criteria [*Van Wychen et al*., 2012, 2014]: (1) due to lateral drag, surface velocities should be faster along glacier centerlines than at margins; (2) flow vectors should be constrained by topography and oriented with surface flow features (e.g., medial moraines); and (3) flow vectors should depict relatively coherent flow units and should not deviate greatly from adjacent vectors.

Mismatches identified using the above criteria were manually removed from the data set, and the velocities were resampled to a 100 m resolution raster using inverse distance-weighting interpolation. Rasters derived from individual image pairs were mosaicked to produce a single raster data set for each individual ice mass and clipped to the extent of version 3.2 of the Global Land Ice Measurements from Space Randolph Glacier Inventory (RGI) for the Canadian High Arctic [*Pfeffer et al*., 2014]. In regions of raster overlap, the lowest velocity value was selected in order to provide a conservative estimate of surface motion, following the methodology of *Short and Gray* [2005] and *Van Wychen et al*. [2012, 2014].

2.2.2. Feature Tracking of Landsat 7 ETM+ Data Sets

An automated, variable correlation block size MATLAB algorithm implemented in the frequency domain (i.e., correlations are performed in the Fourier space rather than in intensity space [*Fitch et al*., 2002]) was developed to derive time series of glacier surface velocities from the Landsat 7 data. This method begins by automatically coregistering all imagery to a common base image (in this case, to imagery acquired in 2000) and then uses a cross-correlation algorithm on coregistered intensity gradient images (similar to *Haug et al*. [2010]) to determine displacements between image pairs. After the images have been matched at the initial correlation block size and the resultant motion vectors have been calculated, a nearest neighbor filter is applied to the velocity field to identify incorrect matches (tolerance for mismatches is user defined). For each incorrect match, the block size is increased and the cross-correlation algorithm is automatically rerun. The process is repeated until an established maximum correlation block size is used. This approach is computationally efficient and effective for determining ice motion on glaciers with large spatial gradients in surface velocities (e.g., tributaries versus main glacier trunks). A comparison of the fixed-block and variable-block image cross-correlation approach for deriving glacier motion is provided by *Sharp et al*. [2014]. Any remaining mismatches were manually removed from the data set using the method described in section 2.2.1, and the final displacements were standardized to annual values.

2.3. Velocity Error Analysis

2.3.1. Speckle Tracking Error Analysis

Errors associated with the speckle tracking method and the random error associated with the cross-correlation technique between coherent complex image chips have been described in previous studies [e.g., *Gray et al*., 2001; *Joughin*, 2002; *Short and Gray*, 2004]. Speckle tracking applied to 24 day repeat imagery with good coherence (>~0.6) provides velocity errors of 2–10 m a^{-1} in the Canadian Arctic [*Short and Gray*, 2005]. In heavily crevassed, faster-flowing regions, where the method reverts to feature tracking, errors of 10–20 m a^{-1} are more likely [*Short and Gray*, 2005]. To determine error bounds for the velocity measurements of each ice mass for each year in this study, velocities were extracted from regions of known zero or near-zero motion. These regions consisted of bedrock outcrops within and adjacent to the ice masses, and ice divides as delineated in version 3.2 of the RGI. Nonzero velocity values derived over apparently stationary features ranged from 3.7 m a^{-1} (standard deviation (SD) = 5.3 m a^{-1}) over Manson Icefield in 2014 to 21.1 m a^{-1} (SD = 7.2 m a^{-1}) over Manson Icefield in 2008 (Table 2). To provide an estimate of confidence in our speckle tracking results, we use the root sum of squares from all the separate sources of error (bedrock outcrops and ice divides) for each ice mass, which yields an uncertainty estimate of ±~8.7 m a^{-1}.

Table 2. Error Analysis Determined From Apparent Motion Over Stationary Regions (Bedrock (BR) and Ice Divides (ID))[a]

	2000		2006	2007	2008	2009	2010	2011		2012		2013		2014		2015	
Ice Mass	BR	ID	BR	BR	BR	BR	BR	BR	ID	BR	ID	BR	ID	BR	ID	BR	ID
Manson	$16.4^{8.5}$	$16.0^{5.3}$		$11.1^{7.4}$	$21.1^{7.2}$	$9.0^{5.3}$				$4.4^{3.7}$	$6.5^{3.6}$	$4.9^{6.6}$	$6.6^{4.7}$	$3.7^{5.3}$	$6.0^{3.7}$	$6.6^{5.1}$	$7.7^{3.6}$
Sydkap										$9.8^{6.5}$	$10.3^{5.4}$	$8.6^{8.2}$	$9.5^{6.1}$	$6.1^{3.5}$	$7.0^{3.7}$	$7.3^{8.6}$	$7.6^{4.0}$
Prince of Wales	$12.0^{9.9}$	$15.4^{8.9}$	$12.3^{13.0}$	$9.3^{9.3}$	$12.1^{10.2}$	$11.1^{5.6}$	$12.1^{6.8}$	$6.9^{6.5}$	$9.2^{5.9}$	$5.9^{4.5}$	$7.7^{5.5}$	$6.2^{4.1}$	$7.8^{5.6}$	$5.0^{4.5}$	$8.5^{5.9}$	$8.0^{6.7}$	$7.0^{5.8}$
Agassiz	$11.0^{8.1}$	$11.2^{5.4}$	$7.3^{7.6}$	$6.1^{7.3}$	$7.7^{6.3}$	$4.7^{4.2}$	$6.1^{9.4}$	$6.2^{3.4}$	$7.8^{4.3}$	$5.2^{4.5}$	$6.1^{2.9}$	$5.9^{4.0}$	$6.0^{3.2}$	$5.7^{4.0}$	$4.7^{2.8}$	$6.7^{9.2}$	$7.6^{4.1}$
Northern Ellesmere	$9.4^{9.0}$	$9.8^{6.3}$	$6.3^{6.4}$	$7.9^{11.8}$	$4.5^{6.8}$	$15.5^{16.1}$	$6.7^{4.2}$	$7.1^{5.0}$	$8.9^{5.2}$	$6.4^{7.1}$	$6.1^{2.6}$	$6.6^{7.4}$	$5.3^{3.7}$	$5.9^{7.9}$	$6.1^{3.4}$	$10.0^{6.2}$	$9.3^{4.4}$
Müller and Steacie	$11.6^{6.6}$	$12.3^{7.5}$	$4.6^{5.0}$	$5.2^{4.7}$	$15.8^{6.2}$	$4.4^{4.4}$	$4.1^{3.4}$	$6.2^{3.7}$	$8.2^{3.4}$	$6.4^{6.6}$	$6.5^{3.2}$	$6.4^{4.1}$	$7.8^{4.3}$	$6.5^{3.5}$	$6.8^{3.8}$	$9.6^{6.6}$	$10.5^{5.7}$

[a]Estimates of ice divides are not possible in 2006–2010 due to surface velocity mosaics that are restricted to the lower regions of ice masses. Superscripts indicate the standard deviation of the data set. Units in m a^{-1}.

2.3.2. Feature Tracking Error Analysis

For feature tracking displacements, the maximum error in the coregistration procedure (determined by extracting maximum displacements over nonmoving terrain) was 0.75 of a pixel (11.25 m) in both the *x* and *y* image directions. There is an additional error associated with how the cross-correlation algorithm picks the subpixel location of the correlation peak, which was quantified as ~0.5 pixels (7.5 m) by finding the location of the peak of a fitted parabolic function using the maximum value of the correlation matrix and the correlation values of the neighbors on either side in both the *x* and *y* direction [*Argyiou and Vlachos*, 2007]. Both of these errors are considered to be independent in the *x* and *y* directions. The resultant error in ice surface velocity derived from feature tracking of a pair of Landsat 7 images is then calculated to be ±19 m a^{-1} by combining the coregistration and correlation peak errors.

2.4. Identification of Surge Features and Terminus Positions

ASTER (15 m resolution) and Landsat 8 OLI (30 m resolution) multispectral images were used to identify features indicative of surge activity such as looped moraines, extensive fresh crevassing, and digitate termini, as described by *Copland et al.* [2003a]. The lack of multitemporal, high-quality elevation data for the Canadian Arctic precludes the identification of glacier geometry changes associated with surges (e.g., reservoir area thinning and receiving area thickening) for most of the region's glaciers, although terminus advance coincident with increases in glacier motion can be used as a proxy for such changes, albeit an imperfect one. Thus, for the larger tidewater-terminating glaciers that experienced significant (>~20 m a^{-1}; described in section 3.3) changes in surface velocity between the beginning and end of the study period, we also used ASTER and Landsat 8 panchromatic data (15 m resolution) to quantify the annual pattern of terminus advance, stagnation or retreat. Positional error in this imagery is assumed to be roughly the size of the image pixel. Monitoring of the terminus positions aids in the determination of whether dynamic changes observed over the period 2000–2014 were associated with changes in the glacier geometry, the patterns of which can be used to infer whether the dynamic changes can be explained in terms of surging, or whether other mechanisms are required.

2.5. Determination of Dynamic Discharge

We define dynamic discharge as the mass passing through a terminus flux gate per unit time. However, our analysis does not account for changes in discharge due to terminus retreat or advance. To compute dynamic discharge, we determine the amount of mass transferred through a cross section near the grounding line of each tidewater glacier within the study region (all flux gates are fixed in space and are located within 1–5 km of the 2014 glacier calving front). To define flux gates, ice thicknesses were derived from airborne-radar measurements made with the Multichannel Coherent RADAR Depth Sounder (MCoRDS) sensor during the NASA Airborne Topographic Mapping (ATM) mission in the spring of 2006 and NASA Operation Icebridge campaigns in 2012 and 2014. Error in the ice depth measurements recorded by the MCoRDS sensor is ~±10 m and provides the value used for the ice thickness error (H_{error}) in equations (1) and (2) below [*Gogineni*, 2012; *Van Wychen et al.*, 2014].

For glaciers where ice thickness measurements were acquired perpendicular to glacier flow (23 of 49 glaciers), a cross-sectional fluxgate was created whereby the terminus width was divided into evenly spaced columns. In limited instances where ice thickness data were missing from parts of the cross section (3 of 23 glaciers), we used a linear interpolation to fill in missing data. Interpolated ice column widths of 20 m were used to be consistent with the measurements provided by MCoRDS. For each column, the measured surface velocities were converted to a depth-averaged value (80% of surface velocity [*Paterson*, 1994] for the lower estimate (Q_{min}) and 100% of surface velocity (which assumes that all flow is by basal slip) for the upper estimate (Q_{max})). Minimum and maximum estimates of discharge were then made for each column width (W) using

$$Q_{min} = (0.8 \times (V - V_{error})) \times (H - H_{error}) \times (W) \quad (1)$$

$$Q_{max} = (V + V_{error}) \times (H + H_{error}) \times (W) \quad (2)$$

where V is surface velocity, V_{error} is the error associated with each velocity data set (Table 2 provides uncertainty estimates for the RADAR velocity data set, while an uncertainty of $\pm 19\,m\,a^{-1}$ is used for velocities derived from Landsat ETM+ imagery), and H is the ice thickness. Both Q_{min} and Q_{max} are then summed across the entire flux gate, and the reported dynamic discharge is the average of the two, with Q_{min} and Q_{max} providing the lower and upper error margins, respectively.

For glaciers where only centerline ice depth measurements are available (26 of 49 glaciers), we used the following parabolic function to create a "U"-shaped fluxgate:

$$H_{interpolated} = \left(\left(10 - C/D_1^2\right) \times \left(D_2^2\right)\right) + C \quad (3)$$

where $H_{interpolated}$ is the interpolated ice thickness measured from the centerline depth to the glacier marginal ice depth of 10 m, C is the measured centerline depth, D_1 is the distance from the centerline to the glacier margin, and D_2 is the distance from the centerline to the center of the interpolated ice column. Ice column thickness was interpolated at 20 m intervals from the centerline to the margins of each glacier.

This method provides approximations of glacier morphology that are consistent with known depth distributions of tidewater glaciers within the Canadian High Arctic [e.g., *Gogineni*, 2012] and is consistent with methods used previously to interpolate fluxgates in the study region [*Van Wychen et al.*, 2014]. *Van Wychen et al.* [2014] compared glacier depths derived using the parabolic interpolation function with those obtained where the actual bedrock form was measured. They found that the modeled geometry tended to underestimate the true cross-sectional area by ~12%.

The RADAR-derived flux estimates do not include summer speedup events (e.g., enhanced motion associated with supraglacial drainage or sea ice buttressing) and are likely to provide conservative estimates of total annual discharge. Flux derived from feature tracking of optical imagery more accurately represents annual mass loss via calving; however it is restricted to ~10–15 glaciers within the region with distinct surface features to track, which provide reliable velocities across the entire terminus flux gate.

2.5.1. Longitudinal Bed Elevation Profiles

To investigate the influence of glacier bed topography on dynamics, we use longitudinal bed elevation profiles collected over the Canadian Arctic in 2000 [*Dowdeswell et al.*, 2004]. These profiles were collected roughly along glacier centerlines using an airborne 100 MHz ice-penetrating RADAR system (details on sensor characteristics and data processing are provided by *Dowdeswell et al.* [2004]). Error associated with the measurements is ~ ±10 m based on the comparison of coincident elevations derived from crossing flight paths.

3. Results

3.1. General Ice Dynamics of Ellesmere and Axel Heiberg Islands

The velocity structure of the Ellesmere Island and Axel Heiberg Island ice caps measured in this study (Figure 1) is consistent with the pattern of ice motion described previously for ice caps in the Canadian High Arctic [e.g., *Van Wychen et al.*, 2014; *Short and Gray*, 2005; *Williamson et al.*, 2008], although the temporal coverage is greatly improved. In general, velocities are low ($<20\,m\,a^{-1}$) in interior regions of ice caps, suggesting that ice in these regions is frozen to the bed and flowing by internal deformation alone. Velocities tend to increase along the main trunk of outlet glaciers as they descend toward glacier termini. These downglacier velocity increases may be linked to a transition from cold to warm basal conditions as ice is channeled into relatively deep and narrow troughs in the ablation area, or to changes in bedrock topography (sills and steps), the

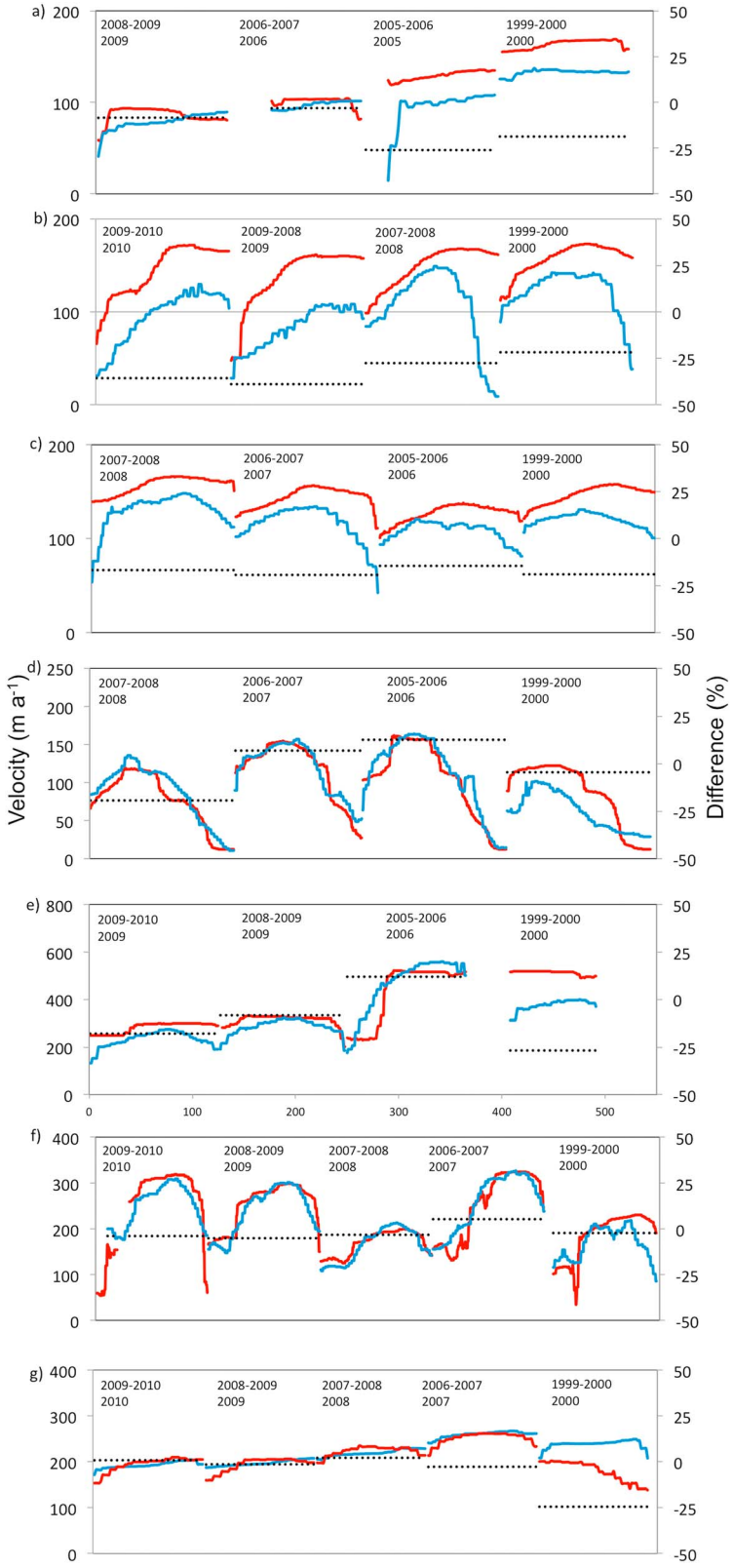

Figure 2. Comparison of near-terminus glacier velocities derived from feature tracking of summer Landsat 7 imagery (annual velocities: red line) and glacier velocities derived from speckle tracking of winter RADARSAT imagery (winter velocities: blue line); black dashed lines indicate the average % difference across the flux gate for (a) Antoinette Glacier, (b) Tuborg Glacier, (c) Cañon Glacier, (d) Cadogan Glacier, (e) Otto Glacier, (f) Wykeham Glacier, and (g) Ekblaw Glacier.

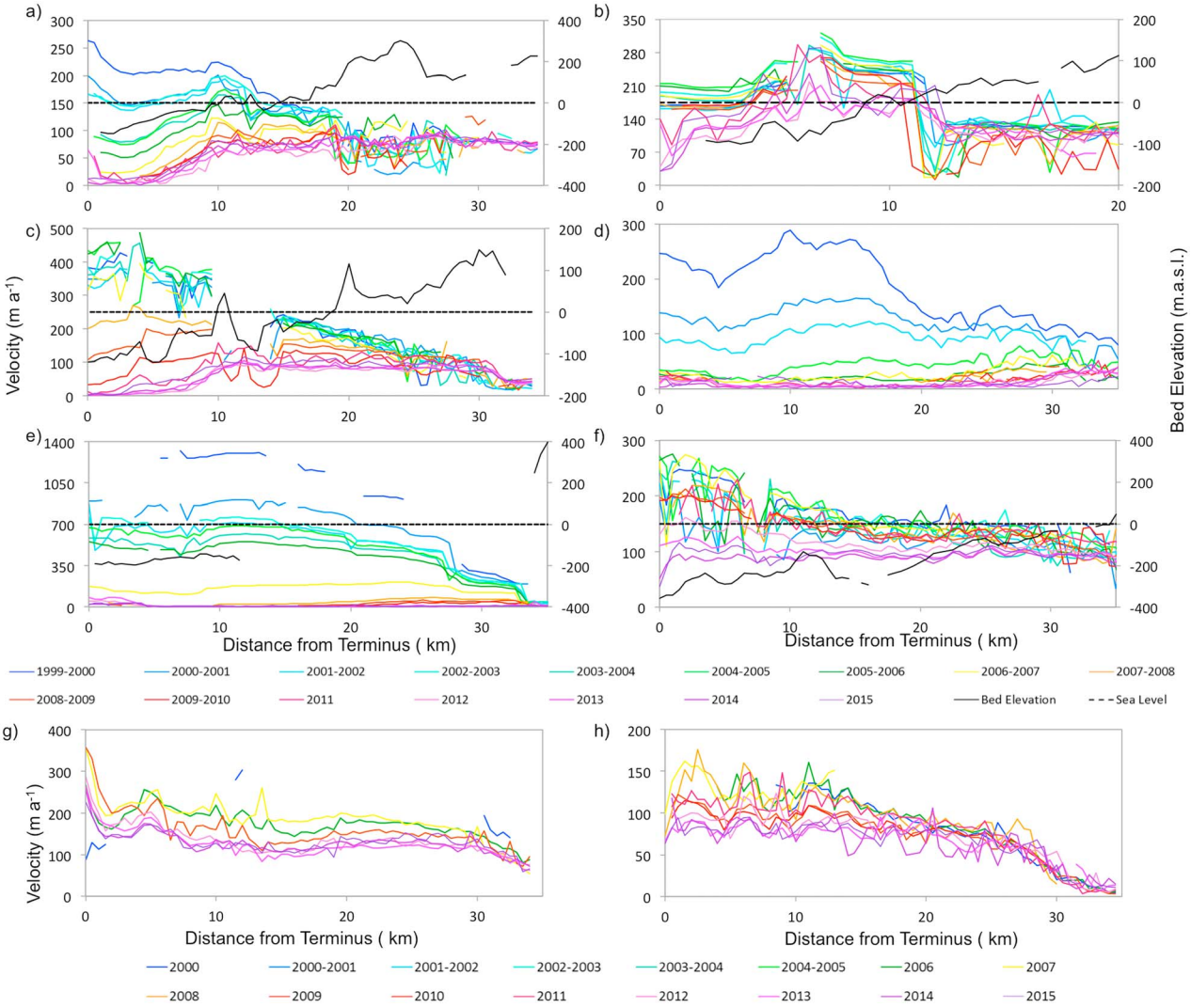

Figure 3. Temporal evolution (slowdown) of centerline glacier surface velocities for (a) Antoinette Glacier, (b) Tuborg Glacier, (c) Eugenie Glacier, (d) Iceberg Glacier, (e) Mittie Glacier, (f) Ekblaw Glacier, (g) Good Friday Bay Glacier, and (h) Middle Glacier. Where available, solid black line indicates glacier bed elevation and dashed black line indicates sea level (both plotted on secondary axis). Note that velocity profiles that span more than 1 year represent displacements derived from feature tracking (i.e., annual velocities) and profiles plotted for a single year represent displacements derived from speckle tracking (i.e., winter velocities).

presence/absence of subglacial sediments, or changes in subglacial sediment type [*Burgess et al.*, 2005; *Copland et al.*, 2003a]. Surface velocities measured in this study rarely exceed 75 m a^{-1} for land-terminating glaciers and 400 m a^{-1} for the terminal regions of tidewater glaciers (notable exceptions are the Otto, Mittie (pre-2004), and Trinity and Wykeham Glaciers). There is a tendency for higher flow rates in glaciers draining the eastern edge of the archipelago that is likely driven primarily by locally high rates of accumulation [*Van Wychen et al.*, 2014; *Koerner*, 2005]. These are associated with the proximity of Baffin Bay, the region's major moisture source, and regional climate patterns that result in relatively high accumulation rates on the seaward margins of ice masses and lower accumulation rates on their more continental margins [*Koerner*, 1979, 2005].

3.2. Comparison of "Winter" (Speckle Tracking) and "Annual" (Feature Tracking) Velocities

To determine how well velocity maps derived from speckle tracking of winter RADARSAT imagery capture annual glacier motion, we differenced them from the annual Landsat 7 feature tracking results for all years with spatial and temporal overlap. Based on a total of 970,803 overlapping points, the winter velocities were ~13.6% (SD = 40%) lower than the annual velocities, which can be explained by enhanced glacier motion during the summer months when (a) surface melt may penetrate to the glacier bed and enhance basal sliding and/or (b) the absence of sea ice/mélange may reduce back pressure on the terminus, facilitating more rapid flow

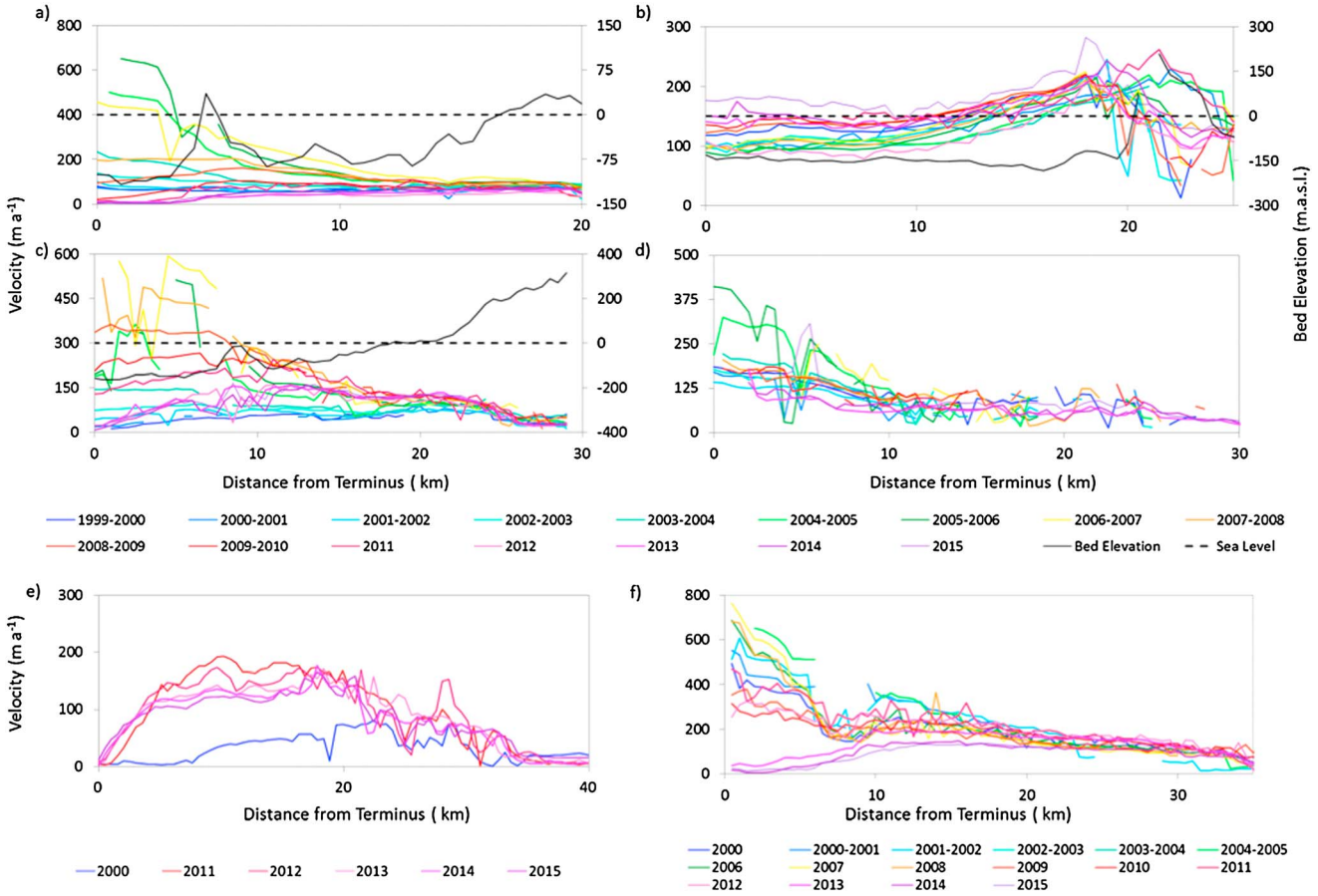

Figure 4. Temporal evolution of centerline glacier surface velocities for (a) Dobbin Glacier, (b) Cañon Glacier, (c) Parrish Glacier, (d) Sydkap Glacier, (e) Chapman Glacier, and (f) Otto Glacier. Where available, solid black line indicates glacier bed elevation and dashed black line indicates sea level (both plotted on secondary axis). Note that velocity profiles that span more than 1 year represent displacements derived from feature tracking (i.e., annual velocities) and profiles plotted for a single year represent displacements derived from speckle tracking (i.e., winter velocities).

across the grounding line of tidewater-terminating glaciers. To assess whether these differences varied at the terminus, we extracted a cross-sectional velocity profile within 5 km of the calving front for seven glaciers with coincident velocity data derived both from RADAR and optical data (Figure 2). Within the lowermost terminus region, the difference between winter and annual velocities becomes larger, with winter speckle tracking velocities typically ~15–25% lower than annual feature tracking results. This suggests that dynamic discharges calculated from speckle tracking velocities are a conservative estimate of annual mass flux.

3.3. Areas of Velocity Change

The annual surface velocity mosaics were differenced from each other to identify regions where significant ($>$~20 m a^{-1}) velocity changes have occurred during the last ~10–15 years. Overall, the majority of glaciers (101 of 117, ~86%) showed no significant velocity changes over the period 1999–2015 (Figure 1). The remaining 16 glaciers exhibited long-term velocity changes in excess of the error associated with the individual data sets and the greater than expected seasonal differences between velocities derived from winter-only data and velocities derived from nearly annually separated imagery. For these glaciers, the glacier centerline velocity structure was plotted separately for glaciers that either slowed down (Figure 3), displayed temporally variable velocities (Figure 4), or sped up (Figure 5). The following discussion focuses on these three sets of glaciers.

3.3.1. Glaciers With Velocity Decrease

Eight of 117 glaciers (~7%) exhibited a significant multiyear reduction in velocity during the observation period (Figure 3 and Table 3). These glaciers are distributed throughout the study region and show no distinct

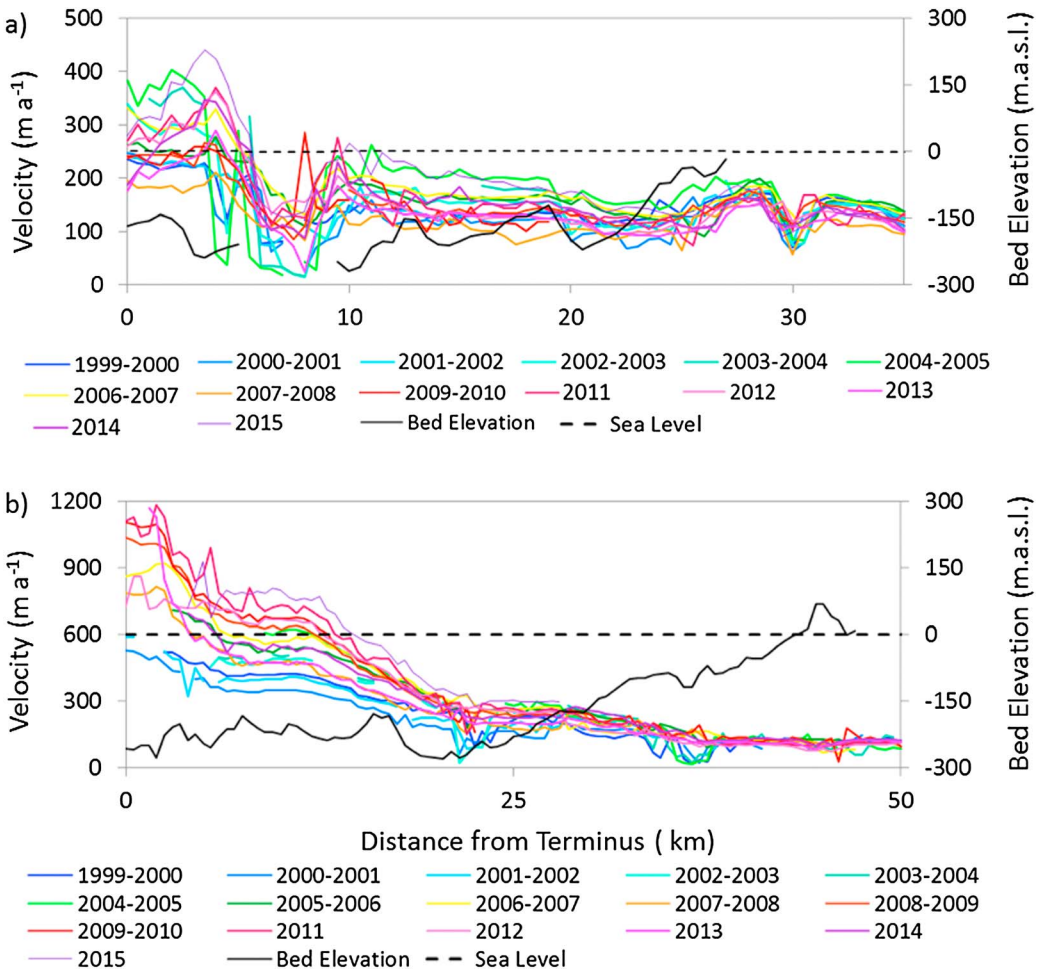

Figure 5. Temporal evolution (speedup) of centerline glacier surface velocities for (a) Wykeham Glacier and (b) Trinity Glacier, both of Prince of Wales Icefield. Solid black line indicates glacier bed elevation; dashed black line indicates sea level (both plotted on secondary axis). Note that velocity profiles that span more than 1 year represent displacements derived from feature tracking (i.e., annual velocities) and profiles plotted for a single year represent displacements derived from speckle tracking (i.e., winter velocities).

spatial pattern, although they are predominantly large and tidewater terminating (Middle Glacier is the only land-terminating glacier in this group). The combined speckle tracking and feature tracking velocities reveal that deceleration of many of the glaciers occurred over a 5–7 year period, and for the glaciers that showed the most dramatic velocity decreases (Antoinette, Eugenie, Iceberg, and Mittie) the glacier became essentially stagnant (velocities $< 20\,\mathrm{m\,a^{-1}}$). The glaciers that slowed down less dramatically (Tuborg, Ekblaw, Good Friday Bay, and Middle) did so over a 5–10 year period, but they are not currently stagnant in their lower regions, which may mean that they are still decelerating.

3.3.2. Glaciers With Variable Velocity Change

Six of 117 glaciers (~5%) exhibited bidirectional velocity changes (speedup followed by slowdown, or vice versa) during the observation period (Figure 4 and Table 3). Dobbin, Parrish, and Sydkap Glaciers (Figures 4a, 4c, and 4d) were nearly stagnant in their terminal regions in the early 2000s, but their velocities all increased to peak between ~2004 and 2006 and then declined gradually to values similar to those observed in the early 2000s by 2013–2015. Velocities in the lowermost ~10 km of Cañon Glacier were ~110–130 m a^{-1} in 1999–2000, decreased to ~80–100 m a^{-1} from 2001 to 2007 and then increased again to ~140–150 m a^{-1} by 2009–2011 (Figure 4b). Notably, in the winter of 2012, Cañon Glacier's surface velocity decreased to ~90–100 m a^{-1} in its lowermost region (and in some locations it had the lowest velocities observed during the entire study period), before returning to speeds of ~140–150 m a^{-1} in 2013 and ~170–180 m a^{-1} in winter 2015.

Journal of Geophysical Research: Earth Surface

10.1002/2015JF003708

Table 3. Dynamic Change, Terminus Response, and Identification of Surface Features Indicative of Surging for the 16 Glaciers That Underwent Significant Velocity Variation Over the 1999–2015 Period

Glacier	Ice Mass	Type	Dynamic Change	Terminus Position	Surge Features
Antoinette	Agassiz	Pulse	Slowdown (~100 m a^{-1} in 2000; stagnant in 2015)	Retreat (~1.1 km: 2002–2014)	
Tuborg[a]	Agassiz	Pulse	Slowdown (~180 m a^{-1} in 2000; slowing to ~90 m a^{-1} in 2015)	Retreat (~2.25 km: 2002–2014)	Digitate terminus
Eugenie	Agassiz	Pulse	Slowdown (~300–400 m a^{-1} 2000; stagnant in 2012–2015)	Retreat (~1.2 km: 2002–2014)	Longitudinal crevassing
Iceberg[a]	Müller	Surge	Slowdown (~75–100 m a^{-1} in 2000; stagnant in 2015)	Retreat (~1.5–2.5 km: 2000–2004)	Looped moraines
Mittie[a]	Manson	Surge	Slowdown (~750 m a^{-1} in 2000; stagnant in 2015)	Retreat (~4 km: 2002–2014)	Heavy terminus crevassing
Ekblaw	Prince of Wales	Pulse	Slowdown (~500 m a^{-1} in 2000; ~100 m a^{-1} in 2015)	Retreat (~0.5 km: 2000–2014)	
Good Friday Bay[a]	Steacie	Surge	Slowdown (~200–300 m a^{-1} in 2006; ~150–200 m a^{-1} in 2015)	Advance (~2 km: 2000–2014)	Extensive crevassing, looped moraines (2014)
Middle[a]	Müller	Surge	Slow down (~165 m a^{-1} in 2000; slowing to ~75 m a^{-1} in 2015)	Advance (~1 km: 2000–2014)	Looped moraines
Dobbin	Prince of Wales	Pulse	Variable (~160–180 m a^{-1} in 2000; ~100–120 m a^{-1} in 2015)	Retreat (0.8 km: 2000–2014)	
Cañon[a]	Agassiz	Pulse	Variable (~100–125 m a^{-1} 2000–2008; ~150–175 m a^{-1} in 2015)	Retreat (~2 km: 2002–2014)	
Parrish[a]	Agassiz	Pulse	Variable (~80 m a^{-1} in 2000; ~200–250 m a^{-1} in 2011; slowing 2012–2015)	Variable (approximately advance ~2 km: ~2000–2012; Retreat 300 m 2012–2014)	
Sydkap	Sydkap	Pulse	Variable (~100 m a^{-1} in 2000; ~400 m a^{-1} in 2006; ~100 m a^{-1} in 2015)	Retreat (1.2 km: 2007–2014)	
Chapman[a]	Northern Ellesmere	Surge	Variable (~40–80 m a^{-1} in 2000; ~150–200 m a^{-1} by 2011)	Stable (2002–2014)	Looped and distorted moraines
Otto[a]	Northern Ellesmere	Surge	Variable (~800 m a^{-1} in lower terminus in 2000; stagnant in 2015)	Retreat (~1.2 km: 2002–2014)	
Wykeham	Prince of Wales	Pulse	Speedup (~200–300 m a^{-1} in 2000; increasing to 500 m a^{-1} by 2015)	Retreat (~1 km: 2000–2014)	
Trinity	Prince of Wales	Accelerating	Speedup (~500–750 m a^{-1} in 2000; 750–1250 m a^{-1} in 2015)	Retreat (~3–4 km: 2000–2014)	

[a]Glaciers that have previously been identified as surge type by *Copland et al.* [2003a].

Chapman Glacier (Figure 4e) had velocities of ~5–50 m a^{-1} in the lowermost 20 km of its main trunk in winter 2000, but by 2011 these had increased to ~200 m a^{-1}. In each subsequent winter from 2011 to 2015 the velocities in the region ~5–20 km upglacier from the glacier terminus decreased, while those in the lowermost ~1–5 km of the glacier increased (the lowermost ~1 km region of Chapman Glacier was nearly stagnant over the entire observation period and may indicate that this region is frozen to its bed). Otto Glacier (Figure 4f) sped up from ~200–400 m a^{-1} in 2000 in its lower ~10 km, to reach peak velocities of ~600–700 m a^{-1} in the winters of 2007 and 2008 in the lowermost 5 km of the glacier. Velocities in this area then declined to ~250–300 m a^{-1} by the winters of 2009 and 2010, and by 2013–2015 this part of the glacier was stagnant.

3.3.3. Glaciers With Velocity Increase

Only 2 of 117 glaciers (~2%) sped up consistently over the observation period. Surface velocities of Wykeham Glacier generally increased over the observation period (Figure 5a), albeit with some year-to-year variability. Velocities were ~250 m a^{-1} over the lowermost 5 km of the glacier from 1999 to 2000, increased to ~350 m a^{-1} in the same region by 2004–2005, and then decreased to a minimum of just under ~200 m a^{-1} in 2007–2008. Surface velocity then increased consistently from 2009 to 2014, reaching up to ~450 m a^{-1} ~5 km upglacier from the calving front in winter 2015 (although the highest near-terminus velocities were observed in 2004–2005).

Trinity Glacier also accelerated over most of the observation period (Figure 5b and Table 3). Velocities were ~300–550 m a^{-1} in the lowermost ~30 km of the main glacier from 1999 to 2002. They increased to ~600–900 m a^{-1} in the summers from 2005 to 2008, and to ~800–1250 m a^{-1} in the winters from 2011 to 2015. The speedup has not been unidirectional, however, as velocities in 2007–2008 were slightly lower than in 2006–2007, and velocities in winter 2013 were lower than those in the winters of 2012 and 2014. Overall, the mean speed of Trinity Glacier has more than doubled over the past decade, and it is currently the fastest flowing glacier in the study region.

3.4. Bed Elevations and Velocity Variability

For glaciers for which bed elevation information is available, the onset location of interannual variability typically occurs immediately downglacier of the location where the bed elevation initially drops below sea level (Figures 3a–3c, 3e, 4a–4c, 4e, and 5). Upglacier of these locations, glacier velocities exhibit little to no interannual variability. Dobbin Glacier (Figure 4a) provides one of the clearest examples of this, as the lowermost ~15 km of the glacier that is grounded below sea level exhibited speedup and slowdown over the observation period, while there was negligible velocity variability in the 5 km section upglacier from the location where bed elevations rise above sea level. This pattern of velocity variability, being mainly restricted to areas where the glacier is grounded below sea level, is also evident on Trinity, Parrish, Wykeham, Antoinette, Tuborg, Eugenie, and Ekblaw Glaciers.

3.5. Patterns of Dynamic Change

Characterizing the spatiotemporal pattern of velocity change provides an opportunity to determine whether faster flow initiated upglacier and propagated toward the terminus or vice versa and can provide insights into the causes of dynamic change. We therefore present maps of the annual surface velocities and interannual velocity differences for Dobbin (Figures 6a and 6b), Parrish (Figures 7a and 7b), and Trinity Glaciers (Figures 8a and 8b). These glaciers have the most continuous velocity records along their entire lengths for computation of interannual velocity changes. The point where the bed of each glacier descends below sea level is also indicated in Figures 6–8 along with sill locations.

For Dobbin Glacier (Figures 6a and 6b), glacier speedup originated in the lowermost terminus region between 2003/2004 and 2004/2005. Between 2004–2005 and 2005–2006 velocities near the terminus changed little, although the region of higher velocities expanded into the region ~4–8 km from the terminus. The slowdown between 2005–2006 and 2006–2007 originated in the lowermost terminus region and spread upglacier. For Parrish Glacier (Figure 7a), the speedup event also began in the lowermost terminus region (within ~7 km of the calving front) in the summers from 2004–2005 to 2006–2007. Velocity differencing (Figure 7b) indicates that the subsequent slowdown also initiated in this area. The patterns of velocity change on both Dobbin and Parrish Glaciers indicate that dynamic variability in both of these glaciers originates, and has the greatest variability, in areas which are grounded below sea level and downglacier of bedrock sills. There is less pronounced dynamic variability in areas where the bed is

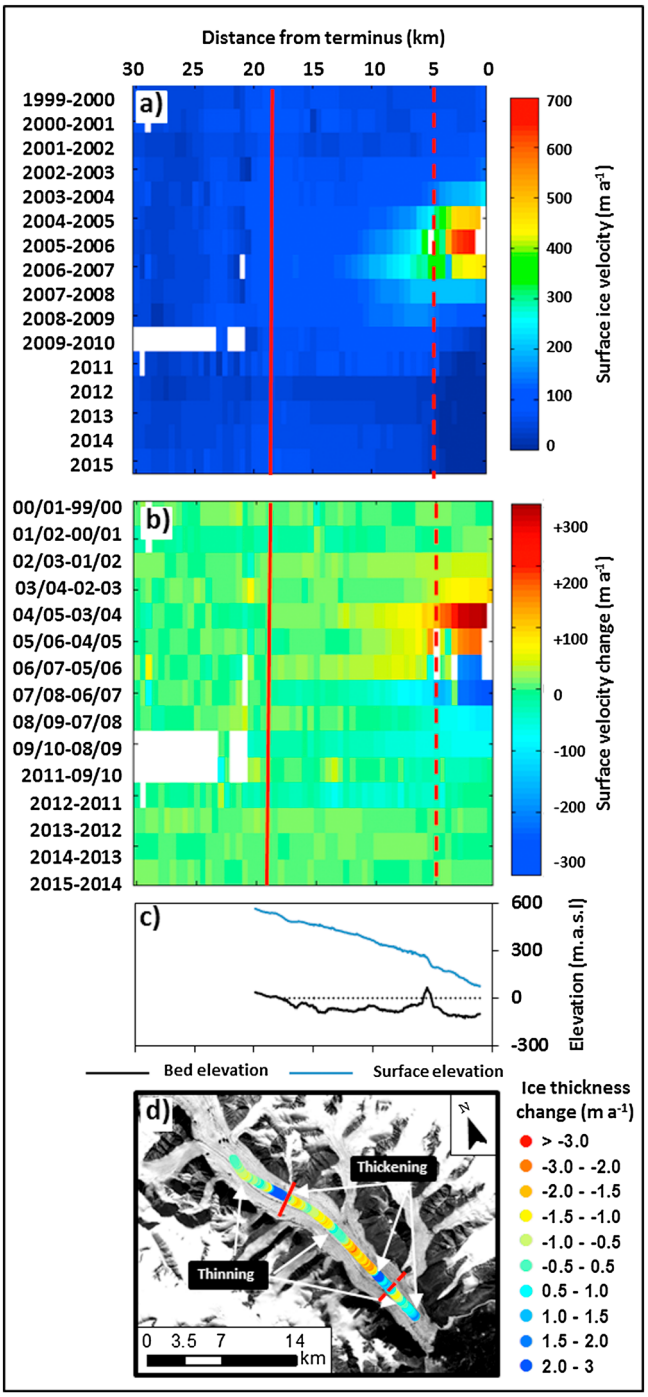

Figure 6. (a) Patterns of annual surface ice velocity extracted every 500 m along the centerline of Dobbin Glacier, (b) patterns of interannual differences in surface ice velocities along the centerline of Dobbin Glacier, (c) surface elevation and bed profile of Dobbin Glacier (black dashed line indicates sea level), and (d) change in centerline ice thickness profiles between 2000 (derived by *Dowdeswell et al.* [2004]) and 2014 (derived by NASA Operation Icebridge McORDS sensor) for Dobbin Glacier; background image: ASTER scene acquired 11 June 2012 (for Figures 6a, 6b, and 6d, solid red lines indicate the location where the bed descends below sea level and dashed red line indicates sill location).

grounded below sea level, but upglacier of the sills. However, the speedup along this portion of the glacier lags behind that of the lowermost terminus region, which is likely due to longitudinal coupling and ice being "pulled" from this region as the terminus accelerates.

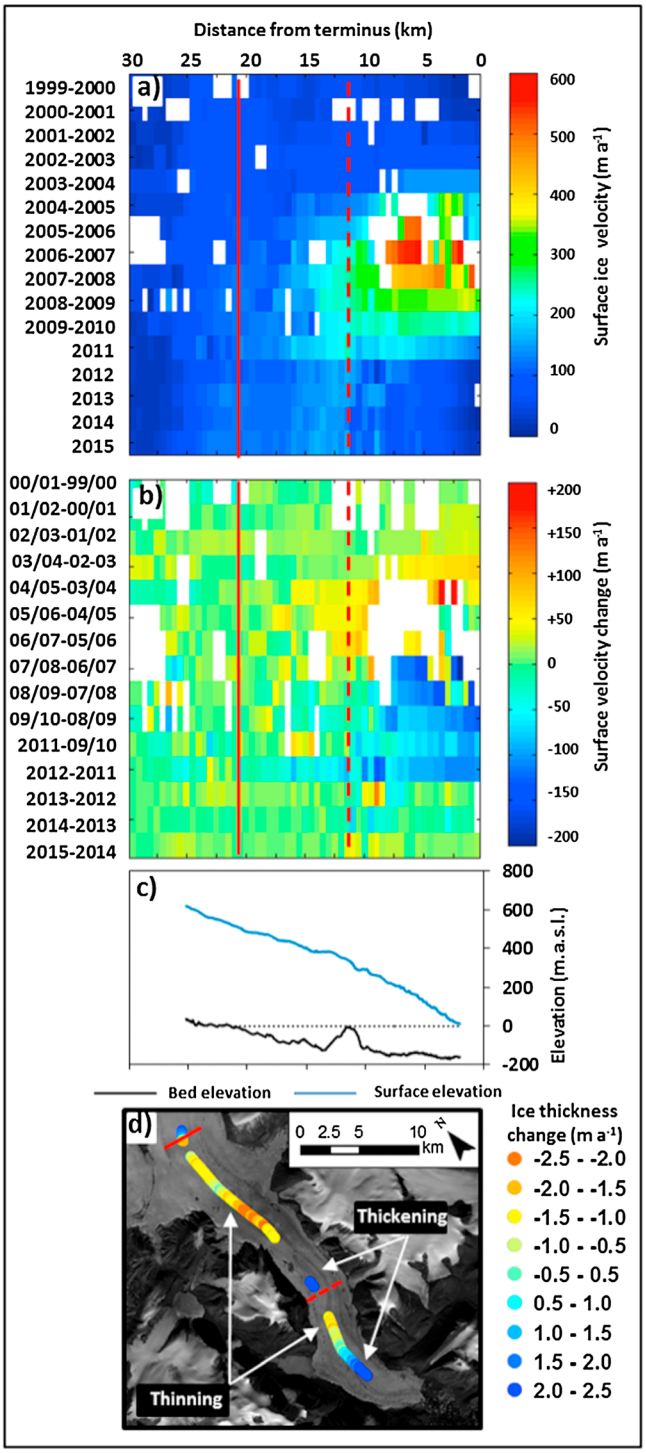

Figure 7. (a) Patterns of annual surface ice velocity extracted every 500 m along the centerline of Parrish Glacier, (b) patterns of interannual differences in surface ice velocities along the centerline of Parrish Glacier, (c) surface elevation and bed profile of Parrish Glacier (black dashed line indicates sea level), and (d) change in centerline ice thickness profiles between 2000 (derived by *Dowdeswell et al.* [2004]) and 2014 (derived by NASA Operation Icebridge McORDS sensor) for Parrish Glacier; background image: ASTER scene acquired 4 August 2013 (for Figures 7a, 7b, and 7d, solid red lines indicate the location where the bed descends below sea level and dashed red line indicates sill location).

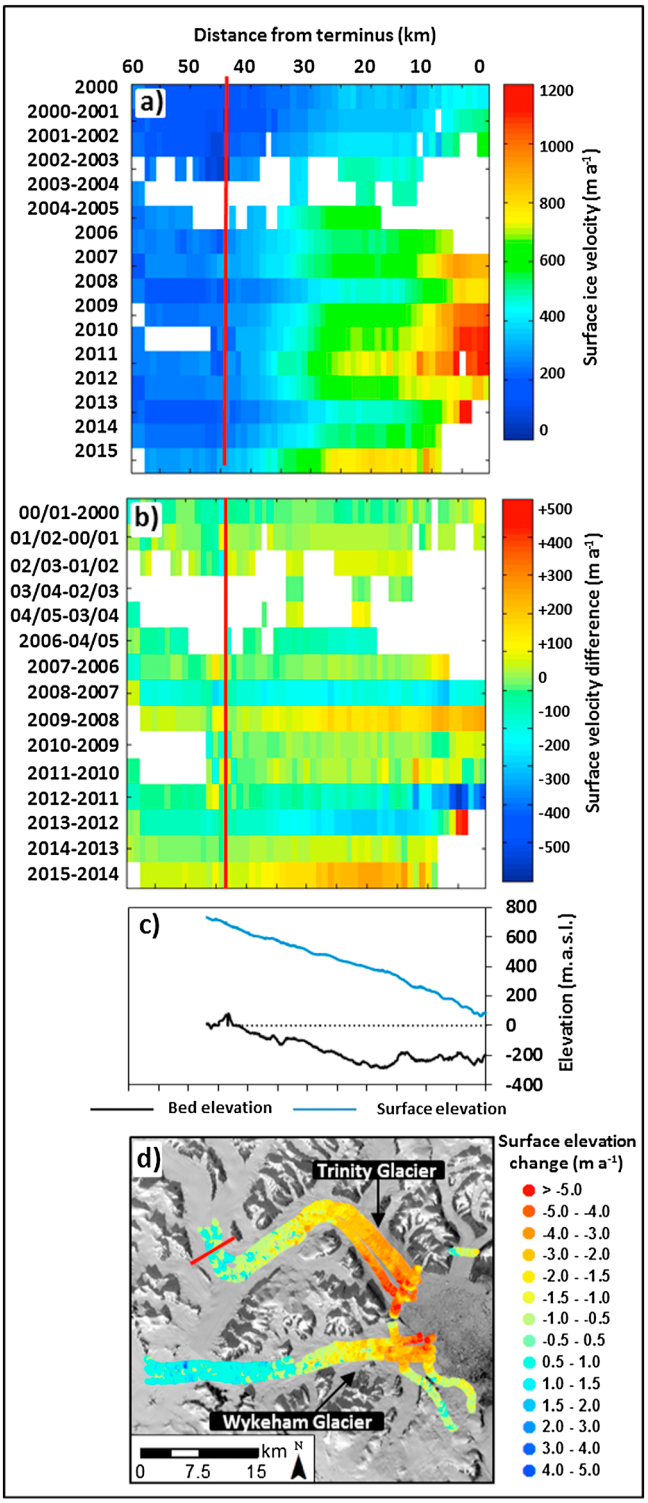

Figure 8. (a) Patterns of annual surface ice velocity extracted every 500 m along the centerline of Trinity Glacier, (b) patterns of interannual differences in surface ice velocities along the centerline of Trinity Glacier, (c) surface elevation and bed profile of Trinity Glacier (black dashed line indicates sea level), and (d) surface elevation change from 2008 (SPOT DEM) and 2014 NASA Operation Icebridge ATM data for Trinity Glacier; background image: Landsat 8 scene acquired 7 September 2014 (for Figures 8a, 8b, and 8d, solid red lines indicate the location where the bed descends below sea level).

For Trinity Glacier (Figures 8a and 8b), we see no evidence of significant velocity variability upglacier of the point where the bed descends below sea level. Rather, it is evident that the lowermost terminus region (~10 km from the calving front) underwent significant speedup from 2006 to 2011 and that this speedup initiated in this part of the glacier. It is also evident that elevated flow speeds have extended progressively farther upglacier over time and that larger areas of the glacier were flowing faster in the latter years of the study period. Unlike Parrish and Dobbin Glaciers, Trinity Glacier does not have a sill (Figure 8c) located in the regions where it is grounded below sea level, which may explain why large regions of it were able to accelerate progressively through the observation period.

3.6. Velocity Fluctuations and Terminus Positions

To understand the causes of the observed changes in motion of the 16 glaciers that underwent significant variations over the study period, it is useful to look at the temporal changes in the terminus position of these glaciers (Table 3). Among the glaciers that advanced, Good Friday Bay and Middle Glaciers advanced by ~2 km and ~1 km, respectively. Parrish Glacier advanced by ~2 km between 2000 and 2012, with the maximum advance occurring between 2000 and 2009. This occurred coincident with a period of faster flow that originated in its terminus region which likely led to longitudinal extension which may explain the terminus advance observed at this time. Between 2012 and 2014 the terminus of Parrish Glacier retreated by ~300 m after velocities across the lower terminus reached stagnation. This retreat was likely caused by an overextension of the terminus region coupled with lower ice velocities which could not replace mass being lost by iceberg calving and surface and/or oceanic melt.

Frontal retreat was the most common terminus behavior within the study region over the observation period, with retreat of ~1–4 km occurring on glaciers which transitioned from high velocities early in the study period to near stagnation in their lowermost terminus regions in later years (e.g., Antoinette, Eugenie, Iceberg, Mittie, Parrish, and Otto glaciers; Table 3). Significant, although generally less, terminus retreat (~0.5–2 km) also occurred on glaciers where near-terminus velocity decreased, but not to the point of terminus stagnation (e.g., Ekblaw and Sydkap Glaciers) and on those where velocity fluctuated during the observation period (e.g., Cañon Glacier). The retreat of these termini may also be linked to overextension due to the advance of the terminus during previous periods of faster flow, with retreat beginning once velocities decrease and flow can no longer replace mass being lost at the glacier front.

Trinity and Wykeham Glaciers are the only glaciers that underwent a significant and near-continuous acceleration throughout the study period that was accompanied by terminus retreat (of up to 4 km for Trinity Glacier; Table 3). This pattern of terminus behavior may be linked to increasing longitudinal extension as the lowermost terminus of the glacier accelerates faster than portions of the trunk located upglacier, leading to thinning of the main glacier trunk and possibly floatation. The pattern of dynamic change for Trinity Glacier shows that the speedup originated in the lowermost terminus the glacier, which is consistent with this interpretation. Chapman Glacier is the only glacier that underwent significant change in dynamics coupled with no appreciable change in terminus position, a pattern similar to the 1990s surge of Bakaninbreen, Svalbard [*Murray et al.*, 1998].

4. Discussion

On the basis of the observations presented above, we identify three primary types of velocity variability (Table 3).

4.1. Surge-Type Flow Variability

We attribute the velocity variability of Mittie, Good Friday Bay, Middle, Iceberg, Otto, and Chapman Glaciers to surging, primarily because each of these glaciers underwent velocity changes of 1 or 2 orders of magnitude above background levels. Otto and Good Friday Bay Glaciers both experienced periods of fast flow in the 1960s [*Hattersley-Smith*, 1969; *Müller*, 1969; *Copland et al.*, 2003a], which suggests a cyclical velocity fluctuation for them. Rapid flow was evident over the entire ~35 km trunk of Iceberg Glacier in 2000. It appears that the subsequent slowdown began and occurred most rapidly in the lowermost terminus region and then spread upglacier until ~2010, at which point the entire glacier trunk was nearly stagnant. Terminus retreat was coincident with the slowdown, a pattern similar to that observed after surges of Otto and Mittie Glaciers. We classify the behavior of Mittie and Middle Glaciers as surge type because terminus advance coincided with the speedup of the main trunk of each glacier and because the velocity patterns indicate

that enhanced surface velocities occurred over nearly their entire lengths. Chapman Glacier is classified as surge type because the peak surface velocities migrated downstream from ~20 to 30 km upglacier from the terminus in 2000, to the region 10–20 km upglacier from the terminus in 2011. This pattern suggests that the Chapman Glacier surged between 2000 and 2011 and that the surge originated upglacier and propagated downglacier but appears to have ceased before activating faster flow in the lowermost terminus region.

Given the 5–10 year active phases and ~30–35 year quiescent phases observed for Otto and Good Friday Bay Glaciers (the only glaciers within the study region for which we have evidence of two active phases to constrain the length of the surge cycle), the surges of these glaciers may be thermally controlled, as has been suggested for surge-type glaciers in Svalbard. More study is required to determine the details of these patterns and how common they are throughout the Canadian Arctic and how they compare to surges observed in Svalbard.

4.2. Pulse-Type Flow Variability

Many of the glaciers within the study region have experienced significant velocity variability, but there is insufficient evidence to definitively classify them as surge type. We therefore identify these glaciers as pulse-type, and apply this designation to Antoinette, Tuborg, Eugenie, Dobbin, Cañon, Parrish, Ekblaw, and Sydkap Glaciers (Table 3). Most of these glaciers exhibited either a multiyear slowdown or a multiyear speedup followed by slowdown during the observation period. The relationship between terminus position and velocity structure is similar to that of the glaciers identified as surge type (i.e., terminus advance as surface ice velocity increases in the terminus region and terminus retreat as the termini slow to stagnation). However, the major distinction between the glaciers identified as pulse type and surge type is that nearly all of the velocity variability of pulse-type glaciers initiates in and propagates upglacier from the lowermost sections of the glacier near the terminus. Another distinction is that the velocity variability is largely restricted to regions where the bed lies below sea level.

Comparison of the longitudinal velocity profiles with bed elevation profiles indicates that velocity variability of pulse-type glaciers is confined to sections of the bed grounded below sea level and is not transmitted upglacier of the point at which the bed rises above sea level. In essence, the longitudinal velocity gradient in the terminus region behaves like a flap attached to a hinge point located where the bed crosses sea level. The fact that elevated surface velocities are not transmitted upglacier of this point is in contrast to the velocity variability of surge-type glaciers, where the entire length of the main glacier trunk is activated during a surge. This suggests that bed elevation may be an important control on the variability of ice motion for pulse-type glaciers in the Canadian High Arctic in that it limits how far velocity variations can propagate upglacier and affect ice motion in the interior of ice masses.

Our repeated velocity mapping captured the acceleration and deceleration phases of "pulse" events on Parrish and Dobbin Glaciers. Both glaciers have nearly coincident (within ~150 m horizontally) ice thickness profiles acquired both before (in 2000) and after (in 2014) the pulse event occurred, allowing investigation of how the glacier geometry in the lower ablation area changed due to the velocity perturbation (Figure 8). To verify the accuracy of these ice thickness measurements, we compared ice elevation changes derived for Dobbin Glacier from ICESat (±0.1 m) [*Gardner et al*., 2011] with those collected within a 150 m radius of the ice thickness flight lines. The average rate of surface elevation change derived from ICESat was $\sim -1.4\,\mathrm{m\,a^{-1}}$ from 2003 to 2009, which if extrapolated to the 2000–2015 period would equate to ~21 m of thinning. Our ice thickness profiles reveal ice thinning of ~17 m in the same region between 2000 and 2014, which is similar to the thinning rate determined from the ICESat data and within the quoted (±10 m) error margins of the ice thickness profiles.

Both Dobbin (Figure 6c) and Parrish (Figure 7c) Glaciers are grounded below sea level for the majority of their ~20 km lengths, but both have a sill that rises above sea level upglacier of their calving front (~4.5–5 km upglacier for Dobbin Glacier and ~8–12 km upglacier for Parrish Glacier). Dobbin (Figure 6d) and Parrish (Figure 7d) Glaciers also have a common pattern of thinning in the region between where the bed first goes below sea level and the sill, with a localized region of thickening coincident with the sill. Downglacier of the sill, both glaciers have an area of thinning that extends roughly half the distance to the calving front and transitions to an area of thickening in the lowermost region of the terminus, particularly for Parrish Glacier. These patterns suggest that the speedup of these glaciers has transferred mass from upglacier locations to regions

above the sill and to the lowermost 3 km of the glacier. Although our data are limited, it is possible that as ice thickens at these locations, it also steepens, which results in increased flow rates until the flux increases enough that it results in a pulse of discharge that is transferred to the terminus region.

Copland et al. [2003a] previously identified Tuborg, Sydkap, and Dobbin Bay Glaciers as "likely or possibly surge type," while all of the other glaciers identified here as pulse type have not previously been classified. *Copland et al*. [2003a] based their classification on the identification of features that suggested past surge activity (e.g., looped moraines, extensive crevassing, shear margins, folding, digitate termini, and terminus retreat), but it is possible that these features could be created from a pulse-type event rather than by surging. Conversely, it is possible that what we identify here as pulse-type events represent a form of surging that is restricted to the lowermost terminus region of tidewater glaciers.

4.3. Consistent Acceleration

Trinity and Wykeham Glaciers, which drain southeast Prince of Wales Icefield, are the only glaciers that sped up fairly consistently throughout the study period. These speedups occurred simultaneously with retreat of both termini (~3–4 km for Trinity Glacier and ~1 km for Wykeham Glacier). This pattern of velocity increase, in conjunction with terminus retreat, is at odds with the behavior of all other glaciers measured in our study region. For other glaciers where we have evidence of speedup, both pulse type and surge type, terminus advance occurred at the same time. We therefore interpret the dynamic changes on Trinity and Wykeham Glaciers as involving a mechanism that is different from that which caused the velocity fluctuations of all other glaciers in this study.

To investigate this further, we compared surface elevations of Trinity and Wykeham Glaciers in 2008 (using a digital elevation model (DEM) derived from SPOT imagery (± ~6 m)) and 2014 (using NASA ATM data obtained during Operation Icebridge (± ~10 cm)) to examine patterns of thickness change over these glaciers (Figure 8d). Our results indicate surface lowering of ~2–5 m a^{-1} in the lowermost ~15 km section of Trinity Glacier. This thinning is similar to the rate of ~3.5 m a^{-1} determined from a comparison of repeat ICESat surface elevation profiles acquired between 2003 and 2009 [*Gardner et al*., 2011]. In comparison, surface elevation changes of two glaciers located within ~8 km and ~15 km of the Trinity/Wykeham calving front (also derived from the 2008 SPOT DEM and the 2014 NASA ATM data) averaged ~−0.61 m a^{-1}, while mass balance measurements and modeling suggest that surface ablation via melting in this area is < 2 m a^{-1} [*Mair et al*., 2009; *Marshall et al*., 2007]. This implies that at least half of the observed thinning rate of the terminus of Trinity Glacier is attributable to changes in dynamics.

This combination of terminus acceleration, thinning, and terminus retreat is similar to that described for tidewater-terminating Helheim Glacier, Greenland, which retreated by ~8 km between 2000 and 2005, while its surface speed increased from ~6–8 km a^{-1} to ~8–11 km a^{-1} in the lowermost ~15 km of the glacier [*Howat et al*., 2005; *Joughin et al*., 2008]. The retreat of Helheim Glacier has been attributed to thinning of the glacier front (either by oceanic or atmospheric forcing, or some combination of the two) that removed longitudinal resistive stresses and initiated faster flow [*Joughin et al*., 2012]. The terminus retreat and acceleration on Trinity and Wykeham Glaciers is also analogous to the retreat pattern of Columbia Glacier, Alaska, which has been attributed to the "retreat phase" of a tidewater glacier cycle [*Meier and Post*, 1987; *Pfeffer*, 2007]. The retreat phase of the tidewater glacier cycle initiates due to accelerated ice flow in the lowermost terminus region, which acts to thin upstream ice and reduce effective pressure at the glacier bed, which in turn allows flow to accelerate and the ice to thin further so that acceleration propagates upglacier from the terminus [*Meier and Post*, 1987; *Pfeffer*, 2007]. It is possible that the prolonged retreat of both Trinity and Wykeham Glaciers (~8 km for Trinity Glacier and ~4 km for Wykeham Glacier) since the 1960s [*Sharp et al*., 2014] has reduced the resistive stresses at their combined front, allowing them to accelerate and thin in recent years. If Trinity Glacier is undergoing a retreat driven by acceleration and thinning leading to glacier flotation then the fact that its bed lies below sea level for ~45 km upglacier from its current calving front, together with the lack of a prominent sill, may make it prone to significant further retreat before restabilization occurs.

4.4. Dynamic Discharge

Given the wide variability in the velocity behavior of individual glaciers described above, an important question is whether the total dynamic discharge has changed significantly over time. To evaluate this, Table 4 presents

Table 4. Temporal Variability in Dynamic Discharge for Individual Glaciers and Ice Masses of the Canadian High Arctic[a]

			Dynamic Discharge (Gt a^{-1})										
Glacier	Latitude	Longitude	2000	2006	2007	2008	2009	2010	2011	2012	2013	2014	2015
Mittie East (CS[b]) and West (CL[b]) Arms	76.85	−79.33	$0.90^{0.25}$		$0.09^{0.05}$	$0.07^{0.07}$	$0.03^{0.03}$			$0.02^{0.02}$	$0.02^{0.02}$	$0.02^{0.02}$	$0.02^{0.02}$
Manson dynamic discharge			$0.90^{0.25}$		$0.09^{0.09}$	$0.07^{0.07}$	$0.03^{0.03}$			$0.02^{0.02}$	$0.02^{0.02}$	$0.02^{0.02}$	$0.02^{0.02}$
Sydkap (CS[b])	76.62	−85.11								$0.02^{0.01}$	$0.02^{0.01}$	$0.03^{0.01}$	$0.04^{0.01}$
Sydkap dynamic discharge										$0.02^{0.01}$	$0.02^{0.01}$	$0.03^{0.01}$	$0.04^{0.01}$
Cadogan (CS[c])	78.23	−76.94	$0.09^{0.03}$	$0.14^{0.03}$	$0.13^{0.03}$	$0.10^{0.03}$		$0.08^{0.02}$	$0.08^{0.02}$	$0.06^{0.02}$	$0.05^{0.02}$	$0.06^{0.02}$	$0.06^{0.02}$
Wyville Thomson (CS[c])	78.42	−75.50	$0.01^{0.01}$							$0.01^{0.01}$	$0.01^{0.01}$	$0.01^{0.01}$	$0.01^{0.01}$
Cadogan South2 (CS[c])	78.39	−75.29	$0.01^{0.01}$								$0.01^{0.01}$	$0.01^{0.01}$	$0.01^{0.01}$
Cadogan South3 (CS[c])	78.38	−75.22									$0.00^{0.01}$	$0.00^{0.01}$	$0.00^{0.01}$
Ekblaw (CS[c])	78.51	−76.71	$0.14^{0.03}$	$0.20^{0.03}$	$0.20^{0.03}$	$0.17^{0.03}$	$0.15^{0.03}$	$0.15^{0.03}$	$0.12^{0.03}$	$0.11^{0.02}$	$0.08^{0.02}$	$0.07^{0.02}$	$0.08^{0.02}$
Tanquary (CL[c])	78.46	−76.08	$0.03^{0.02}$				$0.05^{0.02}$		$0.07^{0.02}$	$0.05^{0.02}$	$0.04^{0.01}$	$0.04^{0.01}$	$0.05^{0.01}$
Leffert (CS_{int}[c])	78.69	−74.92	$0.02^{0.01}$							$0.00^{0.00}$	$0.01^{0.00}$	$0.01^{0.00}$	$0.01^{0.00}$
Palisade (CL[c])	77.39	−80.99	$0.02^{0.01}$							$0.00^{0.00}$	$0.00^{0.00}$	$0.00^{0.00}$	$0.00^{0.00}$
South 2 (CL[c])	77.33	−79.62	$0.01^{0.01}$						$0.01^{0.04}$	$0.02^{0.04}$	$0.02^{0.04}$	$0.02^{0.04}$	$0.02^{0.01}$
South 3 (CL[c])	77.31	−80.30	$0.01^{0.01}$							$0.00^{0.00}$	$0.00^{0.00}$	$0.00^{0.00}$	$0.00^{0.00}$
South 4 (CS[c])	77.33	−79.05							$0.00^{0.00}$	$0.00^{0.00}$	$0.00^{0.00}$	$0.00^{0.00}$	$0.00^{0.00}$
South 5 (CS[c])	77.38	−78.90	$0.00^{0.00}$						$0.00^{0.00}$	$0.00^{0.00}$	$0.00^{0.00}$	$0.00^{0.00}$	$0.00^{0.00}$
South 6 (CS[c])	77.37	−78.93	$0.00^{0.00}$						$0.00^{0.00}$	$0.00^{0.00}$	$0.00^{0.00}$	$0.00^{0.00}$	$0.00^{0.00}$
South 7 (CS[c])	77.41	−78.76	$0.02^{0.01}$						$0.03^{0.01}$	$0.02^{0.01}$	$0.02^{0.01}$	$0.02^{0.01}$	$0.02^{0.01}$
Stygge (CS[c])	78.77	−78.24	$0.01^{0.01}$						$0.01^{0.01}$	$0.01^{0.01}$	$0.01^{0.01}$	$0.01^{0.01}$	$0.01^{0.01}$
Sands (CL[c])	78.95	−78.06							$0.00^{0.00}$	$0.01^{0.01}$	$0.01^{0.01}$	$0.01^{0.01}$	$0.01^{0.01}$
Trinity (CS[c])	77.97	−78.57	$0.38^{0.08}$	$0.75^{0.12}$	$0.84^{0.14}$	$0.66^{0.11}$	$0.92^{0.15}$	$0.94^{0.15}$	$1.05^{0.17}$	$0.90^{0.14}$	$0.71^{0.12}$	$0.95^{0.15}$	$1.02^{0.16}$
Wykeham (CS[c])	77.89	−78.61	$0.17^{0.04}$	$0.25^{0.05}$	$0.29^{0.05}$	$0.18^{0.04}$	$0.25^{0.05}$	$0.25^{0.05}$	$0.32^{0.05}$	$0.31^{0.05}$	$0.30^{0.05}$	$0.37^{0.06}$	$0.41^{0.07}$
Talbot (CS_{int}[c])	78.00	−78.24	$0.02^{0.01}$	$0.01^{0.01}$	$0.01^{0.01}$	$0.01^{0.01}$	$0.01^{0.01}$	$0.01^{0.01}$	$0.01^{0.01}$	$0.00^{0.01}$	$0.00^{0.01}$	$0.00^{0.01}$	$0.00^{0.01}$
Unnamed1 (CL[c])	77.98	−77.36	$0.02^{0.01}$					$0.01^{0.01}$	$0.01^{0.01}$	$0.00^{0.00}$	$0.01^{0.01}$	$0.00^{0.00}$	$0.00^{0.00}$
Unnamed1 South (CS_{int}[c])	77.90	−77.92	$0.04^{0.01}$				$0.03^{0.01}$	$0.04^{0.01}$	$0.03^{0.01}$	$0.03^{0.01}$	$0.02^{0.01}$	$0.03^{0.01}$	$0.02^{0.01}$
MacMillian (CL[c])	78.52	−75.31	$0.01^{0.01}$							$0.01^{0.01}$	$0.01^{0.01}$	$0.01^{0.01}$	$0.01^{0.01}$
South Margin (CS[c])	77.71	−77.88	$0.06^{0.05}$	$0.02^{0.01}$	$0.02^{0.01}$	$0.02^{0.02}$	$0.03^{0.02}$	$0.01^{0.01}$	$0.07^{0.05}$	$0.06^{0.06}$	$0.06^{0.06}$	$0.08^{0.06}$	$0.06^{0.06}$
Prince of Wales dynamic discharge			$0.92^{0.36}$	$1.19^{0.25}$	$1.49^{0.27}$	$1.14^{0.51}$	$1.44^{0.29}$	$1.49^{0.29}$	$1.99^{0.38}$	$1.60^{0.42}$	$1.37^{0.42}$	$1.70^{0.45}$	$1.80^{0.44}$
Antoinette (CS[d])	80.81	−76.30	$0.04^{0.01}$	$0.01^{0.01}$	$0.01^{0.01}$		$0.01^{0.01}$	$0.01^{0.01}$	$0.01^{0.01}$	$0.00^{0.00}$	$0.00^{0.00}$	$0.00^{0.00}$	$0.01^{0.01}$
Cañon (CL[c])	79.68	−79.64	$0.04^{0.01}$	$0.03^{0.01}$	$0.03^{0.01}$	$0.03^{0.01}$	$0.04^{0.01}$			$0.04^{0.01}$	$0.06^{0.01}$	$0.06^{0.01}$	$0.07^{0.02}$
d'Iberville (CL[c])	80.56	−77.92	$0.01^{0.01}$	$0.01^{0.01}$			$0.01^{0.01}$	$0.01^{0.01}$	$0.01^{0.01}$	$0.01^{0.01}$	$0.01^{0.01}$	$0.01^{0.01}$	$0.01^{0.01}$
Eugenie (CL[c])	79.82	−74.93	$0.11^{0.02}$						$0.00^{0.01}$	$0.00^{0.01}$	$0.00^{0.01}$	$0.00^{0.01}$	$0.00^{0.01}$
John Richardson (CL[c])	80.23	−72.41	$0.01^{0.01}$						$0.00^{0.01}$	$0.00^{0.01}$	$0.00^{0.01}$	$0.00^{0.01}$	$0.00^{0.01}$
Parrish (CL[c])	79.57	−77.18	$0.02^{0.01}$						$0.05^{0.01}$	$0.01^{0.01}$	$0.01^{0.01}$	$0.01^{0.01}$	$0.01^{0.01}$
Sawyer Bay (CS[d])	79.36	−78.05	$0.01^{0.01}$	$0.01^{0.01}$		$0.01^{0.01}$				$0.01^{0.01}$	$0.01^{0.01}$	$0.01^{0.01}$	$0.01^{0.01}$
Tuborg (CL[c])	80.89	−76.14	$0.03^{0.01}$	$0.03^{0.01}$	$0.03^{0.01}$		$0.03^{0.01}$	$0.03^{0.01}$	$0.04^{0.01}$	$0.02^{0.01}$	$0.03^{0.01}$	$0.03^{0.01}$	$0.03^{0.01}$
Dobbin (CL[c])	79.89	−74.34	$0.02^{0.01}$						$0.00^{0.01}$	$0.00^{0.01}$	$0.00^{0.01}$	$0.00^{0.01}$	$0.00^{0.01}$
Unnamed4 (CL[c])	80.07	−72.39	$0.01^{0.01}$						$0.02^{0.01}$	$0.01^{0.01}$	$0.01^{0.01}$	$0.01^{0.01}$	$0.01^{0.01}$
Agassiz dynamic discharge			$0.30^{0.11}$	$0.09^{0.05}$	$0.07^{0.03}$	$0.04^{0.02}$	$0.09^{0.04}$	$0.05^{0.03}$	$0.13^{0.08}$	$0.10^{0.09}$	$0.13^{0.09}$	$0.13^{0.09}$	$0.15^{0.11}$
Iceberg (CL[c])	79.43	−92.37	$0.03^{0.01}$	$0.00^{0.00}$	$0.00^{0.00}$	$0.01^{0.01}$	$0.00^{0.00}$	$0.01^{0.01}$	$0.01^{0.01}$	$0.00^{0.00}$	$0.00^{0.00}$	$0.00^{0.00}$	$0.00^{0.00}$
Good Friday Bay (CL[c])	78.55	−91.76			$0.08^{0.01}$		$0.07^{0.01}$			$0.06^{0.01}$	$0.05^{0.01}$	$0.05^{0.01}$	$0.05^{0.01}$
Müller & Steacie dynamic discharge			$0.03^{0.01}$	$0.00^{0.00}$	$0.08^{0.01}$	$0.01^{0.01}$	$0.07^{0.01}$	$0.01^{0.01}$	$0.01^{0.01}$	$0.06^{0.01}$	$0.05^{0.01}$	$0.05^{0.01}$	$0.05^{0.01}$

Journal of Geophysical Research: Earth Surface

10.1002/2015JF003708

Table 4. (continued)

Glacier	Latitude	Longitude	Dynamic Discharge (Gt a^{-1})												
			2000	2006	2007	2008	2009	2010	2011	2012	2013	2014	2015
Disraeli (CL[c])	82.67	−72.50	$0.01^{0.01}$						$0.01^{0.01}$	$0.02^{0.01}$	$0.01^{0.01}$	$0.02^{0.01}$	$0.01^{0.01}$
Disraeli North (CL[c])	82.84	−70.79	$0.01^{0.01}$						$0.01^{0.01}$	$0.02^{0.01}$	$0.01^{0.01}$	$0.01^{0.01}$	$0.01^{0.01}$
DeVries (CL[c])	82.01	−79.60							$0.01^{0.01}$	$0.01^{0.01}$	$0.01^{0.01}$	$0.01^{0.01}$	$0.01^{0.01}$
M'Clintock (CL[c])	82.43	−76.15							$0.01^{0.01}$	$0.01^{0.01}$	$0.01^{0.01}$	$0.01^{0.01}$	$0.01^{0.01}$
Marine (CS[d])	82.24	−81.72	$0.01^{0.01}$						$0.01^{0.01}$	$0.01^{0.01}$	$0.01^{0.01}$	$0.01^{0.01}$	$0.01^{0.01}$
Marine North (CS[d])	82.42	−82.54	$0.02^{0.01}$						$0.01^{0.01}$	$0.00^{0.01}$	$0.01^{0.01}$	$0.01^{0.01}$	$0.02^{0.01}$
Milne (CL[c])	82.44	−80.22	$0.07^{0.02}$						$0.06^{0.01}$	$0.06^{0.01}$	$0.05^{0.01}$	$0.05^{0.01}$	$0.06^{0.02}$
Otto (CL[c])	81.30	−84.70	$0.11^{0.02}$	$0.15^{0.03}$	$0.17^{0.03}$	$0.15^{0.03}$	$0.09^{0.02}$	$0.07^{0.01}$	$0.11^{0.02}$	$0.09^{0.02}$	$0.01^{0.01}$	$0.00^{0.01}$	$0.01^{0.01}$
Vanier (CL[c])	82.14	−80.75	$0.01^{0.01}$						$0.01^{0.01}$	$0.01^{0.01}$	$0.01^{0.01}$	$0.01^{0.01}$	$0.01^{0.01}$
Yelverton (CL[c])	81.84	−79.43	$0.12^{0.02}$						$0.06^{0.01}$	$0.07^{0.01}$	$0.08^{0.02}$	$0.08^{0.02}$	$0.08^{0.02}$
Northern Ellesmere dynamic discharge			$\mathbf{0.36^{0.11}}$	$\mathbf{0.15^{0.03}}$	$\mathbf{0.17^{0.03}}$	$\mathbf{0.15^{0.03}}$	$\mathbf{0.09^{0.02}}$	$\mathbf{0.07^{0.01}}$	$\mathbf{0.30^{0.11}}$	$\mathbf{0.30^{0.11}}$	$\mathbf{0.21^{0.11}}$	$\mathbf{0.21^{0.11}}$	$\mathbf{0.23^{0.12}}$
Total regional dynamic discharge			$2.51^{0.84}$	$1.43^{0.33}$	$1.90^{0.43}$	$1.41^{0.64}$	$1.72^{0.39}$	$1.62^{0.34}$	$2.43^{0.58}$	$2.08^{0.64}$	$1.80^{0.66}$	$2.14^{0.69}$	$2.29^{0.71}$

[a]Ice thickness data sources are specified in the succeeding footnotes. Fluxgate method: CS = cross section, CS_{int} = cross section with interpolated ice thickness values to fill in partial missing data, and CL = centerline method. Superscript notation presents (±) uncertainty for each estimate in Gt a^{-1}.
[b]The 2006 NASA Operation Icebridge.
[c]The 2014 NASA Operation Icebridge.
[d]The 2012 NASA Operation Icebridge.

the dynamic discharge derived from RADAR velocities for all tidewater glaciers of Axel Heiberg and Ellesmere Islands with available data from 2000 and 2006–2015 and Table 5 presents the dynamic discharge derived from feature tracking velocities from 1999 to 2010 for 17 glaciers located on Axel Heiberg and Ellesmere Islands. The mean annual discharge calculated for 2000 and from 2011 to 2015 when RADAR imagery was available for the majority of the region's outlet glaciers was 2.21 ± 0.68 Gt a^{-1}. However, the majority of glaciers have been losing less mass via dynamic discharge in recent years due to the dominance of glacier slowdown across the study region. Notable exceptions are the rapid increase in dynamic discharge from Trinity and Wykeham glaciers, which have increased from a combined total of 0.55 ± 0.12 Gt a^{-1} in 2000 to 1.43 ± 0.23 Gt a^{-1} in 2015. These glaciers alone currently account for ~62% of the total regional mass loss via dynamic discharge, and their recent discharge increases approximately offset the reduction in dynamic discharge from the rest of the region's marine-terminating glaciers. Our results indicate that ~10 glaciers account for ~70% of the total dynamic discharge in a given year (similar to *Van Wychen et al.* [2014] for glacier discharges of the Queen Elizabeth Islands as a whole in 2012), although which 10 glaciers account for this discharge varies over time. This variability in glacier dynamic discharge necessitates the continued monitoring of all major tidewater glaciers within the study region to identify the primary sources of iceberg discharge each year.

5. Conclusions

Speckle tracking of pairs of RADARSAT-1/RADARSAT-2 imagery and feature tracking of Landsat 7 optical image scenes has allowed detection and quantification of dynamic change of all major glaciers on Axel Heiberg and Ellesmere Islands over the period 1999–2015. When combined with a record of terminus positions and surface features indicative of surging, our analysis updates the inventory of surge-type glaciers originally completed by *Copland et al.* [2003a]. Based on our observations, we identify Otto, Chapman, Good Friday Bay, Iceberg,

Journal of Geophysical Research: Earth Surface

10.1002/2015JF003708

Table 5. Temporal Variability in Dynamic Discharge for Individual Glaciers and Ice Masses of the Canadian High Arctic[a]

			Dynamic Discharge (Gt a^{-1})										
Glacier	Latitude	Longitude	1999–2000	2000–2001	2001–2002	2002–2003	2003–2004	2004–2005	2005–2006	2006–2007	2007–2008	2008–2009	2009–2010
Manson Icefield													
Mittie East (CS[b])	76.85	−79.33	$1.03^{0.13}$	$0.83^{0.13}$	$0.66^{0.11}$	$0.75^{0.12}$	$0.60^{0.10}$	$0.67^{0.11}$	$0.51^{0.09}$	$0.18^{0.04}$			
Sydkap Ice Cap													
Sydkap (CS[c])	76.62	−85.11	$0.04^{0.01}$	$0.03^{0.01}$	$0.04^{0.03}$	$0.04^{0.01}$	$0.03^{0.01}$	$0.05^{0.01}$	$0.05^{0.01}$		$0.04^{0.01}$	$0.04^{0.01}$	$0.04^{0.01}$
Prince of Wales Icefield													
Cadogan (CS[d])	78.23	−76.94	$0.09^{0.03}$	$0.06^{0.02}$	$0.07^{0.03}$	$0.09^{0.03}$	$0.10^{0.03}$	$0.11^{0.03}$	$0.12^{0.03}$	$0.11^{0.03}$	$0.09^{0.03}$	$0.07^{0.02}$	$0.8^{0.03}$
Ekblaw (CS[d])	78.81	−76.71	$0.13^{0.03}$	$0.12^{0.03}$	$0.15^{0.03}$	$0.05^{0.01}$	$0.11^{0.02}$	$0.16^{0.03}$	$0.12^{0.02}$				
Trinity (CS[d])	77.97	−78.57	$0.47^{0.09}$	$0.35^{0.07}$	$0.43^{0.08}$								
Wykeham (CS[d])	77.89	−78.61	$0.11^{0.03}$	$0.12^{0.03}$	$0.12^{0.03}$	$0.16^{0.03}$	$0.14^{0.03}$	$0.19^{0.04}$	$0.11^{0.02}$				
Agassiz Ice Cap													
Antoinette (CS[b])	80.81	−76.30	$0.06^{0.02}$	$0.05^{0.01}$	$0.04^{0.01}$	$0.05^{0.01}$	$0.03^{0.01}$	$0.04^{0.01}$	$0.03^{0.01}$	$0.02^{0.01}$	$0.01^{0.01}$	$0.01^{0.01}$	$0.01^{0.01}$
Cañon (CL[d])	79.68	−79.64	$0.05^{0.01}$	$0.04^{0.01}$	$0.04^{0.01}$	$0.04^{0.01}$	$0.04^{0.01}$	$0.04^{0.01}$	$0.04^{0.01}$	$0.04^{0.01}$	$0.04^{0.01}$	$0.05^{0.02}$	$0.05^{0.01}$
d'Iberville (CL[d])	80.56	−77.92	$0.01^{0.01}$	$0.01^{0.01}$	$0.01^{0.01}$	$0.01^{0.01}$	$0.01^{0.01}$	$0.01^{0.01}$	$0.01^{0.01}$	$0.01^{0.01}$	$0.01^{0.01}$		$0.01^{0.01}$
Eugenie (CL[d])	79.82	−74.93	$0.12^{0.03}$	$0.12^{0.03}$	$0.11^{0.03}$	$0.13^{0.03}$	$0.12^{0.03}$	$0.14^{0.03}$	$0.14^{0.03}$	$0.12^{0.03}$	$0.07^{0.02}$	$0.04^{0.01}$	$0.01^{0.01}$
John Richardson (CL[d])	80.23	−72.41											
Parrish (CL[d])	79.57	−77.18	$0.01^{0.01}$	$0.02^{0.01}$	$0.02^{0.01}$	$0.03^{0.01}$	$0.05^{0.01}$	$0.05^{0.01}$	$0.06^{0.01}$		$0.11^{0.02}$	$0.11^{0.02}$	$0.09^{0.02}$
Tuborg (CL[d])	80.89	−76.14	$0.05^{0.01}$	$0.05^{0.01}$	$0.05^{0.01}$	$0.06^{0.01}$	$0.06^{0.01}$	$0.06^{0.01}$	$0.04^{0.01}$	$0.05^{0.01}$	$0.05^{0.01}$	$0.05^{0.01}$	$0.05^{0.01}$
Dobbin (CL[d])	79.89	−74.34	$0.02^{0.01}$	$0.01^{0.01}$	$0.02^{0.01}$	$0.03^{0.01}$	$0.04^{0.01}$	$0.08^{0.01}$		$0.07^{0.01}$	$0.04^{0.01}$	$0.02^{0.01}$	$0.01^{0.01}$
Unnamed4 (CL[d])	80.07	−72.39	$0.01^{0.01}$	$0.02^{0.01}$	$0.01^{0.01}$	$0.01^{0.02}$	$0.02^{0.01}$	$0.01^{0.01}$	$0.01^{0.01}$	$0.01^{0.01}$	$0.01^{0.01}$	$0.01^{0.01}$	$0.01^{0.01}$
Müller Ice Cap													
Iceberg (CL[d])	79.43	−92.37	$0.06^{0.01}$	$0.03^{0.01}$	$0.02^{0.01}$			$0.01^{0.01}$	$0.01^{0.01}$	$0.01^{0.01}$	$0.00^{0.01}$	$0.01^{0.01}$	$0.00^{0.01}$
Northern Ellesmere Icefield													
Otto (CL[d])	81.30	−84.70	$0.11^{0.02}$	$0.11^{0.02}$	$0.11^{0.02}$			$0.08^{0.01}$					

[a]Ice thickness data sources are specified in the succeeding footnotes. Fluxgate method: CS = cross section, CS_{int} = cross section with interpolated ice thickness values to fill in partial missing data, and CL = centerline method. Superscript notation presents (±) uncertainty for each estimate in Gt a^{-1}.
[b]The 2012 NASA Operation Icebridge.
[c]The 2006 NASA Operation Icebridge.
[d]The 2014 NASA Operation Icebridge.

Middle, and Mittie Glaciers as surge type. Our analysis also expands on the inventory of *Copland et al*. [2003a] by identifying new pulse-type and "consistent acceleration" classifications to better describe observed velocity variability within the Canadian High Arctic.

Pulse-type glaciers share some characteristics with surge-type glaciers, such as periods of speedup and slowdown, and terminus advance coincident with acceleration, but the key difference is that all of their velocity variability appears to be restricted to their lowermost terminus region that is grounded below sea level. We observe very little year to year variability in ice motion on pulse-type glaciers upglacier of the point where the glacier bed rises above sea level, suggesting that velocity variability is limited by how far it can be transmitted upglacier. Comparison of bed elevation and ice thickness profiles for Dobbin and Parrish Glaciers from before and after a pulse event suggests that increased basal friction over sills leads to compressive ice flow and localized ice thickening upstream of the sill which may be important for causing localized steepening in the vicinity of the sill and initiating accelerated motion in the lowermost terminus regions of pulse-type glaciers. More investigation is required to better understand the drivers of dynamic change for these glaciers and what role the glacier bed properties and geometry may play in regulating ice motion.

The marked speedup of Trinity and Wykeham Glaciers, which has been accompanied by prolonged terminus thinning and retreat, suggests that the velocity variability on these glaciers is not due to surging or pulsing, but rather driven by variations in the stability of the main trunks of both glaciers. As a consequence, we classify these glaciers as displaying consistent acceleration. The pattern of terminus retreat and acceleration for these two glaciers is similar to that displayed by both Helheim Glacier (Greenland) and Columbia Glacier (Alaska), which has been attributed to reductions in resistive stresses at the glacier front that allow the glacier to accelerate and thin, and we may be witnessing the beginning of the retreat phase of a tidewater glacier cycle.

By combining velocities with ice thickness measurements, we provide the most comprehensive record of temporal variability in dynamic ice discharge from Axel Heiberg and Ellesmere Islands to date. Mean dynamic discharge is $2.21 \pm 0.68\,\mathrm{Gt\,a^{-1}}$, with a low value of $1.80 \pm 0.66\,\mathrm{Gt\,a^{-1}}$ in 2013 and high value of $2.51 \pm 0.84\,\mathrm{Gt\,a^{-1}}$ in 2000. Ten glaciers account for ~70% of total ice discharge in any given year, but exactly which glaciers are responsible varies over time due to the high level of velocity variability observed. Total dynamic discharge from surge-type and pulse-type glaciers has generally decreased over time due to many large tidewater glaciers transitioning into periods of slower flow. However, the reduction in total regional dynamic discharge from these glaciers has been offset by the increase in discharge due to the acceleration of the Trinity and Wykeham Glaciers in recent years, which together accounted for ~60% of all dynamic discharge from 2011 to 2014. Due to the widespread speedup and evidence of dynamically induced thinning of the Trinity Glacier there is a great need to better understand the drivers of the recent acceleration of this glacier.

Acknowledgments

We thank NSERC (Discovery Grants and Northern Research supplements to L.C. and M.S.), Canada Foundation for Innovation, Ontario Research Fund, ArcticNet, Ontario Graduate Scholarship, and Polar Continental Shelf Program for funding. Support to D.B. is provided through the Climate Change Geosciences Program, Earth Sciences Sector, Natural Resources Canada (20150295). RADARSAT imagery is made available from the Alaska Satellite Facility, archives at Natural Resources Canada and the RADARSAT-2 Natural Resources Canada data allocation. We thank Julian Dowdeswell and Toby Benham for providing ice thickness and bed elevation profiles utilized by this study and acknowledge support from UK NERC for grants GR3/12469 and NE/K004999 to J.D.

References

Argyiou, V., and T. Vlachos (2007), On the estimation of subpixel motion using phase correlation, *J. Electron. Imaging*, *16*(3), 033018–033018-8, doi:10.1117/1.2762230.

Benn, D. I., and D. J. A. Evans (2010), *Glaciers and Glaciation*, 2nd ed., 802 pp., Arnold, London, U. K.

Bingham, R., P. Nienow, and M. Sharp (2003), Intra-annual and intra-seasonal flow dynamics of a High Arctic polythermal valley glacier, *Ann. Glaciol.*, *37*, 181–188.

Boon, S., and M. Sharp (2003), The role of hydrologically-driven ice fracture in drainage system evolution on an Arctic glacier, *Geophys. Res. Lett.*, *30*(18), 1916, doi:10.1029/2003GL018034.

Burgess, D. O., M. Sharp, D. W. F. Mair, J. A. Dowdeswell, and T. J. Benham (2005), Flow dynamics and iceberg calving rates of Devon Ice Cap, Nunavut, Canada, *J. Glaciol.*, *51*(173), 219–230.

Christoffersen, P., R. Mugford, K. J. Heywood, I. Joughin, J. A. Dowdeswell, J. P. M. Syvitski, A. Luckman, and T. J. Benham (2011), Warming of waters in an East Greenland fjord prior to glacier retreat: Mechanisms and connection to large-scale atmospheric forcing, *Cryosphere*, *5*, 701–714, doi:10.5194/tc-5-701-2011.

Clarke, G. K. C. (1987), Fast glacier flow: Ice streams, surging, and tidewater glaciers, *J. Geophys. Res.*, *92*(B9), 8835–8841, doi:10.1029/JB092iB09p08835.

Copland, L., M. Sharp, and J. A. Dowdeswell (2003a), The distribution and flow characteristics of surge-type glaciers in the Canadian High Arctic, *Ann. Glaciol.*, *36*, 73–81.

Copland, L., M. Sharp, and P. Nienow (2003b), Links between short-term velocity variations and the subglacial hydrology of a polythermal glacier, *J. Glaciol.*, *49*, 407–414.

Dowdeswell, J. A., G. S. Hamilton, and J. O. Hagen (1991), The duration of the active phase on surge-type glaciers: Contrasts between Svalbard and other regions, *J. Glaciol.*, *37*(127), 388–400.

Dowdeswell, J. A., T. J. Benham, M. R. Gorman, D. O. Burgess, and M. Sharp (2004), Form and flow of the Devon Island ice cap, Canadian Arctic, *J. Geophys. Res.*, *109*, F02002, doi:10.1029/2003JF000095.

Fitch, A. J., A. Kadyrov, W. J. Christmas, and J. Kittler (2002), Orientation correlation, in *Electronic Proceedings of the 13th British Machine Vision Conference*, edited by D. Marshall and P. L. Rosin, pp. 133–142, British Machine Vision Association, Cardiff, U. K.

Gardner, A. S., M. Moholdt, B. Wouters, G. J. Wolken, D. O. Burgess, M. Sharp, J. G. Cogley, C. Braun, and C. Labine (2011), Sharply increased mass loss from glaciers and ice caps in the Canadian Arctic Archipelago, *Nature*, *473*(7347), 357–360, doi:10.1038/nature10089.
Gogineni, P. (2012), *Radar Depth Sounder Data Products*, Digital media, Lawrence, Kansas. [Available at http://data.cresis.ku.edu/.]
Gray, A. L., N. Short, K. E. Mattar, and K. C. Jezek (2001), Velocities and flux of the Filchner Ice Shelf and its tributaries determined from speckle tracking interferometry, *Can. J. Remote Sens.*, *27*(3), 193–206.
Hattersley-Smith, G. (1969), Recent observations on the surging of Otto Glacier, Ellesmere Island, *Can. J. Earth Sci.*, *6*(4), 883–889.
Haug, T., A. Kääb, and P. Skvarca (2010), Monitoring ice shelf velocities from repeat MODIS and Landsat data—A method study on the Larsen C ice shelf, Antarctic Peninsula, and 10 other ice shelves around Antarctica, *Cryosphere*, *4*, 161–178, doi:10.5194/tc-4-161-2010.
Holland, D. M., R. H. Thomas, B. de Young, M. H. Ribergaard, and B. Lyberth (2008), Acceleration of Jakobshavn Isbrae triggered by warm subsurface ocean waters, *Nat. Geosci.*, *1*, 659–664, doi:10.1038/ngeo316.
Howat, I. M., I. Joughin, S. Tulaczyk, and S. Gogineni (2005), Rapid retreat and acceleration of Helheim Glacier, east Greenland, *Geophys. Res. Lett.*, *32*, L22502, doi:10.1029/2005GL024737.
Joughin, I. (2002), Ice-sheet velocity mapping: A combined interferometric and speckle tracking approach, *Ann. Glaciol.*, *34*, 195–201.
Joughin, I., I. Howat, R. B. Alley, G. Ekstrom, M. Fahnestock, T. Moon, M. Nettles, M. Truffer, and V. C. Tsai (2008), Ice-front variation and tidewater behavior on Helheim and Kangerdlugssuaq Glaciers, Greenland, *J. Geophys. Res.*, *113*, F01004, doi:10.1029/2007JF000837.
Joughin, I., R. B. Alley, and D. M. Holland (2012), Ice-sheet response to oceanic forcing, *Science*, *338*(6111), 1172–1176, doi:10.1126/science.1226481.
Kamb, B. (1987), Glacier surge mechanism based on linked cavity configuration of the basal water conduit system, *J. Geophys. Res.*, *92*(B9), 9083–9100, doi:10.1029/JB092iB09p09083.
Koerner, R. M. (1979), Accumulation, ablation, and oxygen isotope variations on the Queen Elizabeth Island Ice Caps, Canada, *J. Glaciol.*, *22*(86), 25–41.
Koerner, R. M. (2005), Mass balance of glaciers in the Queen Elizabeth Islands, Nunavut, Canada, *Ann. Glaciol.*, *42*, 417–423, doi:10.3189/172756405781813122.
Mair, D., D. O. Burgess, M. Sharp, J. A. Dowdeswell, T. J. Benham, S. Marshall, and F. Cawkwell (2009), Mass balance of the Prince of Wales Icefield, Ellesmere Island, Nunavut, Canada, *J. Geophys. Res.*, *114*, F02011, doi:10.1029/2008JF001082.
Marshall, S., M. Sharp, D. O. Burgess, and F. Anslow (2007), Surface temperature lapse rate variability on the Prince of Wales Icefield, Ellesmere Island, Canada: Implications for regional-scale downscaling of temperature, *Int. J. Climatol.*, *27*, 385–398.
Meier, M. F., and A. Post (1987), Fast tidewater glacier, *J. Geophys. Res.*, *92*(B9), 9051–9058, doi:10.1029/JB092iB09p09051.
Müller, F. (1969), Was the Good Friday Glacier on Axel Heiberg Island surging?, *Can. J. Earth Sci.*, *6*(4), 891–894, doi:10.1139/e69-091.
Murray, T., J. A. Dowdeswell, D. J. Drewry, and I. Frearson (1998), Geometric evolution and ice dynamics during a surge of Bakaninbreen, Svalbard, *J. Glaciol.*, *44*(147), 263–272.
Murray, T., T. Strozzi, A. Luckman, H. Jiskoot, and P. Christakos (2003), Is there a single surge mechanism? Contrasts in dynamics between glacier surges in Svalbard and other regions, *J. Geophys. Res.*, *108*, B52237, doi:10.1029/2002JB001906.
Murray, T., et al. (2010), Ocean regulation hypothesis for glacier dynamics in southeast Greenland and implications for ice sheet mass changes, *J. Geophys. Res.*, *115*, F03026, doi:10.1029/2009JF001522.
Paterson, W. S. B. (1994), *The Physics of Glaciers*, 3rd ed., Elsevier, Oxford.
Pfeffer, W. T. (2007), A simple mechanism for irreversible tidewater glacier retreat, *J. Geophys. Res.*, *112*, F03S25, doi:10.1029/2006JF000590.
Pfeffer, W. T., et al. (2014), The Randolph Glacier Inventory: A globally complete inventory of glaciers, *J. Glaciol.*, *60*, 537–552, doi:10.3189/2014JoG13J176.
Rosen, P., S. Hensley, I. Joughin, S. Madsen, E. Rodriguez, and R. Goldstein (2000), Synthetic aperture radar interferometry, *Proc. IEEE: Trans. Geosci. Remote Sens.*, *88*(3), 333–382, doi:10.1109/5.838084.
Sharp, M., et al. (2014), Remote sensing of recent glacier changes in the Canadian Arctic, in *Global Land Ice Measurements from Space*, edited by J. S. Kargel et al., chap. 9, pp. 205–228, Praxis-Springer, Berlin, doi:10.1007/978-3-540-79818-7_9.
Short, N. H., and A. L. Gray (2004), Potential for RADARSAT-2 interferometry: Glacier monitoring using speckle tracking, *Can. J. Remote Sens.*, *30*(3), 504–509.
Short, N. H., and A. L. Gray (2005), Glacier dynamics in the Canadian High Arctic from RADARSAT-1 speckle tracking, *Can. J. Remote Sens.*, *31*(3), 225–239.
Thomson, L. I., G. R. Osinski, and C. S. L. Ommanney (2011), Glacier change on Axel Heiberg Island, Nunavut, Canada, *J. Glaciol.*, *57*(206), 1079–1086, doi:10.3189/002214311798843287.
Van Wychen, W., L. Copland, L. Gray, D. O. Burgess, B. Danielson, and M. Sharp (2012), Spatial and temporal variation of ice motion and ice flux from Devon Ice Cap, Nunavut, Canada, *J. Glaciol.*, *58*(210), 657–664, doi:10.3189/2012JoG11J164.
Van Wychen, W., D. O. Burgess, L. Gray, L. Copland, M. Sharp, J. A. Dowdeswell, and T. J. Benham (2014), Glacier velocities and dynamic ice discharge from the Queen Elizabeth Islands, Nunavut, Canada, *Geophys. Res. Lett.*, *41*, 484–490, doi:10.1002/2013GL058558.
Williamson, S., M. Sharp, J. Dowdeswell, and T. Benham (2008), Iceberg calving rates from northern Ellesmere Island ice caps, Canadian Arctic, 1999–2003, *J. Glaciol.*, *54*(186), 391–400, doi:10.3189/002214308785837048.